Renewable Energy 256 (2026) 123991

Contents lists available at ScienceDirect

Renewable Energy

journal homepage: www.elsevier.com/locate/renene

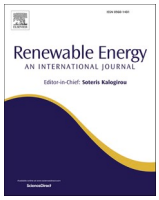

Origin and resource potential of hydrothermal H_2 and CH_4 degassing along the Xianshuihe strike-slip fault, eastern Tibetan Plateau: Insights from H_2-H_2O-CH_4-CO_2 isotope geochemistry

Jiao Tian [a,b], Yinlei Hao [c], Yingchun Wang [d], Dawei Liao [e], Lantian Xing [f], Chunhui Cao [f], Ying Li [a,b], Xiaocheng Zhou [a,b,*], Zhonghe Pang [g,**]

[a] United Laboratory of High-Pressure Physics and Earthquake Science, Institute of Earthquake Forecasting, China Earthquake Administration, Beijing, 100036, China
[b] Key Laboratory of Earthquake Forecasting and Risk Assessment, Ministry of Emergency Management, Beijing, 100036, China
[c] Guangdong Open Laboratory of Geospatial Information Technology and Application, Guangzhou Institute of Geography, Guangdong Academy of Sciences, Guangzhou, 510070, China
[d] State Key Laboratory of Oil and Gas Reservoir Geology and Exploitation, Chengdu University of Technology, Chengdu, 610059, China
[e] Sinopec Petroleum Exploration and Production Research Institute, Beijing, 102206, China
[f] Northwest Institute of Eco-Environment and Resources, Chinese Academy of Sciences, Lanzhou, 730000, China
[g] State Key Laboratory of Lithospheric and Environmental Coevolution, Institute of Geology and Geophysics, Chinese Academy of Sciences, Beijing, 100029, China

ARTICLE INFO

Keywords:
Hydrogen formation
Methane formation
Fault-controlled geothermal system
Tibetan plateau

ABSTRACT

The exploration of natural H_2 and CH_4 in geothermal systems has gained attention due to their potential as low-carbon, high-temperature energy sources. These gases are commonly found in tectonically active regions, such as the Tibetan Plateau, but their origins remain poorly understood. This study investigates the hydrogeological and geochemical processes behind H_2 and CH_4 formation in the seismically active Xianshuihe Fault Zone (XSHF) on the eastern Tibetan Plateau, focusing on isotopic exchanges in the H_2-H_2O-CH_4-CO_2 system. We highlight the presence of H_2 and CH_4 in hydrothermal volatiles from continental orogenic belts lacking mafic or ultramafic rocks. Our findings show that: (1) H_2 is primarily produced by the hydrolysis of silicate minerals on fault surfaces, driven by geothermal circulation in regions with strong seismicity; (2) CH_4 forms from the thermal metamorphism of organic matter in sediments, not abiotic processes; (3) the Kangding Yulingong geothermal system hosts a thermal reservoir at 2 km depth, with a well (2006 m) directly penetrating the reservoir, a novel discovery. While large-scale gas reservoirs are limited, the study highlights the potential of geothermal H_2 and CH_4, contributing insights for exploring renewable energy in continental orogenic regions worldwide.

1. Introduction

In recent years, naturally occurring molecular hydrogen (H_2) and methane (CH_4) have attracted increasing attention due to their significant impact on Earth's geological and biological history, as well as their relevance in the search for extraterrestrial life [1–3]. These gases can sustain chemosynthetic communities by driving metabolic processes and supporting biomass production [4], making these microbial ecosystems potential analogs of early life on Earth [3]. Moreover, the discovery of H_2 and CH_4 on other planetary bodies has heightened their significance in astrobiology, emphasizing prebiotic chemistry topics such as the hydrogen-based origin of life and methane's role as a precursor to life [5]. From an energy perspective, geologically produced H_2 and CH_4 are emerging as promising extractable resources, gaining importance as the global energy transition shifts from high-carbon to low- or non-carbon systems to address climate change [3,6]. Notably, the calorific values of H_2 (1.43×10^8 J/kg) and CH_4 (5.04×10^7 J/kg) [7] significantly exceed those of coal (2.56×10^7 J/kg) [8] and petroleum (4.44×10^7 J/kg) [9].

In nature, abiotic H_2 and CH_4 are often found in volcanic regions and geothermal systems [10,11]. Unlike microbial and thermogenic hydrocarbons, the formation of abiotic CH_4 generally follows three main pathways: (1) water-rock interactions, (2) magmatic and post-magmatic processes, and (3) primordial methane delivered by meteorites during

* Corresponding author. United Laboratory of High-Pressure Physics and Earthquake Science, Institute of Earthquake Forecasting CEA, Beijing, 100036, China.
** Corresponding author.
E-mail addresses: zhouxiaocheng188@163.com (X. Zhou), z.pang@mail.iggcas.ac.cn (Z. Pang).

https://doi.org/10.1016/j.renene.2025.123991
Received 6 December 2024; Received in revised form 8 July 2025; Accepted 11 July 2025
Available online 15 July 2025

Earth's accretion and preserved in the mantle [12]. Key reactions include metal carbide methanation, carbonate metamorphism, and Fischer-Tropsch Type (FTT) reactions [13]. In high-temperature environments (>300 °C), such as magmatic or late-magmatic processes, hydrogen in water acts as an electron acceptor, whereas in most crustal settings, molecular hydrogen serves as the primary reducing agent [14]. Although over 20 processes have been linked to natural abiotic H_2 production on Earth [15], serpentinization of ultramafic rocks is most frequently cited to explain high-grade hydrogen resources across various environments. These include gas seeps in the Zambales Ophiolite, Philippines [16], the Chimaera seep in Turkey [17], deep subsurface aquifers within the Columbia River Basalt Group, USA [18], hyperalkaline springs in Genova, Italy [19], and fluid inclusions in subducted ophicarbonates [11]. Similar processes are observed in vent fluids from the Lost City Hydrothermal Field [20] and the Rainbow Hydrothermal Field [21,22] along the mid-Atlantic Ridge, as well as in low-temperature hot springs along the eastern coast of China [23]. During water-rock interactions, Fe(II) in minerals such as olivine, orthopyroxene, or other ophiolitic rocks (e.g., gabbro, dunite, harzburgite, and lherzolite) is oxidized to Fe(III), facilitating the reduction of water to H_2 [24]. The H_2 produced can then react with carbon species such as CO_2, CO, carbonate or bicarbonate, originating from mantle-derived volatile or crustal metamorphic processes, resulting in the formation of abiotic CH_4 and higher hydrocarbons (e.g., C_2H_6, C_3H_8) [14,19].

However, mechanism of hydrogen production by serpentinization and methane production by FTT reaction do not fully account for the presence of H_2 and CH_4 in hydrothermal volatiles emitted from continental orogenic belts that lack mafic or ultramafic rocks. For example, the Himalaya-Tibet orogen, formed by the collision between the Indian and Asian plates, contains numerous geysers, boiling springs, bubbling springs, and steaming grounds [25,26]. However, the origin of H_2 and CH_4 in these hydrothermal emissions remains unclear. Previous studies have reported the highest volumetric concentrations of H_2 and CH_4 in these regions as follows: 0.0001 % H_2 and 0.85 % CH_4 in the western Himalayan syntaxis [27]; 1.34 % H_2 and 28.23 % CH_4 on the central Tibetan Plateau [28–33]; 0.27 % H_2 and 15.76 % CH_4 in Yunnan Province, southeastern Tibetan Plateau [34,35]; and 2.90 % H_2 and 7.28 % CH_4 in Sichuan Province, on the eastern edge of the plateau [36–40]. Many of these CH_4 samples exhibit δ^{13}C-CH_4 values higher than −25 ‰, indicating a likely abiotic origin [12]. However, the spatial distribution of H_2 and CH_4 (Fig. 1a and b) does not align with the ophiolitic massifs exposed along major suture zones, such as the IYS and BNS sutures in central Tibet [41], or the Ganzi-Litang, Jinshajiang, and Lancangjiang sutures in the eastern plateau [42]. This misalignment suggests that serpentinization and Fischer-Tropsch Type (FTT) reactions alone cannot fully explain the observed H_2 and CH_4 emissions across the Tibetan Plateau. Furthermore, the limited number of studies on hydrothermal H_2 and CH_4 emissions from these springs, combined with the scarcity of isotopic data, has hindered a deeper understanding of their formation mechanisms.

This study investigates the formation of hydrothermal H_2 and CH_4 released from the XSHF, the most active lithospheric-scale strike-slip fault along the eastern edge of the Tibetan Plateau (Fig. 1c). By systematically analyzing the chemical composition and isotopic ratios (e.g. $^3He/^4He$, $^4He/^{20}Ne$, $^{13}C_{CO2}$, $^{13}C_{CH4}$, δD_{CH4}, δD_{H2}, δD_{H2O}, and $\delta^{18}O_{H2O}$) in gas and water samples from 26 hot springs, we explore the origin and evolution of these hydrothermal volatiles in relation to the geological and tectonic context of the XSHF.

2. Geological setting

The Tibetan-Himalayan orogen is the largest mountain chain on Earth. It was formed by the tectonic collision between the Indian and Eurasian plates following the closure of the Neo-Tethys Ocean around 50 million years ago [43]. As a result, the Indian plate has moved approximately 3200 km northward at the Eastern Syntaxis [44], and the crust in this region has thickened to about 60 km [45]. Situated on the eastern edge of the Tibetan Plateau, the Western Sichuan Plateau lies within the influence of the Eastern Himalayan Syntaxis. This intense tectonic activity has generated widespread high-temperature geothermal manifestations along lithospheric-scale strike-slip faults, such as the Xianshuihe Fault (XSHF), the Longmenshan Fault (LTF), and the Jinshajiang Fault. Among these, the XSHF is one of the most active intracontinental faults globally, with an average slip rate of 2–12 mm per year [46]. It plays a crucial role in accommodating the convergence between the Indian and Eurasian plates [47]. The XSHF forms the southeastern segment of the Yushu-Ganzi-Xianshuihe fault system,

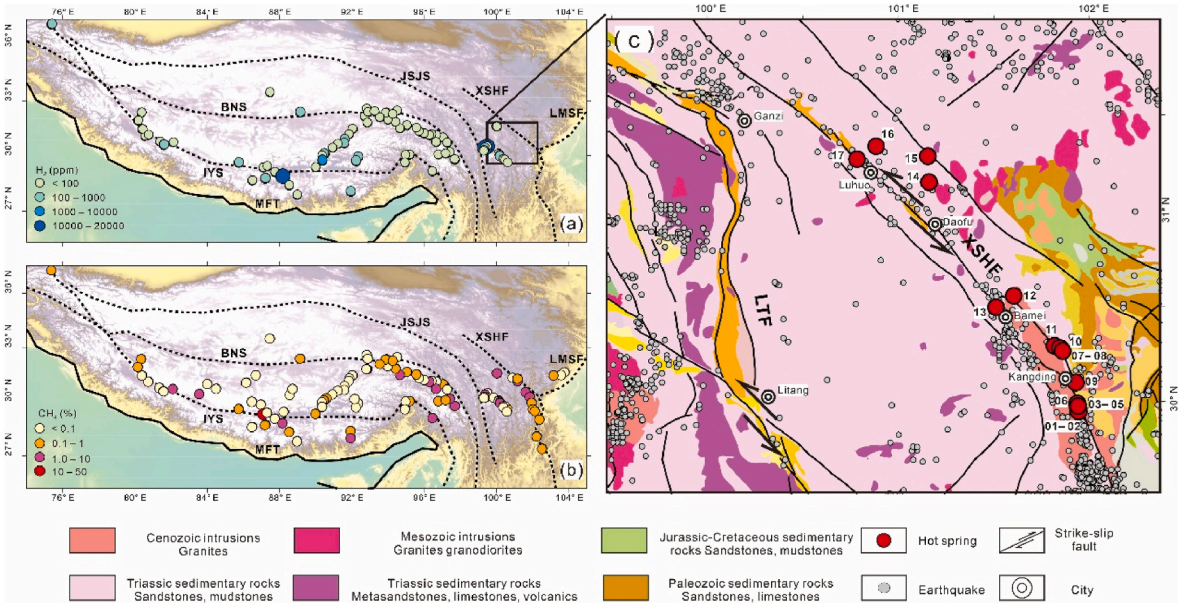

Fig. 1. (a) Summary of the H_2 and (b) CH_4 contents reported in previous studies about the Tibetan Plateau; (c) a geological sketch map of near the XSHF. Abbreviations for faults are as follows: MFT, the Main Frontal thrust; IYS, the Indus-Yarlung suture; BNS, the Bangong-Nujiang suture; JSJS, the Jinshajiang suture; LMSF, the Longmenshan Fault; LTF, the Litang Fault.

which serves as the geological and geophysical boundary between the Bayankala (Songpan-Ganzi) block and the Sichuan-Yunnan block [48]. As shown in Fig. 1c, it extends from Ganzi in the north, passing through Luhuo, Daofu, Kangding, and stretching southward to Shimian, covering a distance of up to 300 km with a dip angle of ~80° [49]. Over the past 300 years, the XSHF has been the site of four major earthquakes with magnitudes exceeding 7.0. Notable events include the Yushu earthquake (Ms 7.1) in 2010 and the Kangding earthquake (Ms 6.4) in 2014, both directly associated with this fault [50,51]. The NW-striking XSHF runs almost parallel to the LTF, and both faults curve southeastward [52]. Geophysical and seismic studies indicate that the crustal thickness near Kangding is approximately 50 km, increasing to 60 km further north near Bamei [53–55].

Along the XSHF, the sedimentary strata are dominated by Triassic sandstones and mudstones with minor Paleozoic sandstones and limestones, Jurassic-Cretaceous sandstones and mudstones. Granitic plutons also distributed along this deep fault, implying the anatexis process in the crust which was triggered in the compressed shear zone [56,57]. Based on the reported ages of the granites [58], they can be divided into two groups (Fig. 1c): (1) Mesozoic Triassic granites (~230 Ma – ~ 204 Ma), granites are associated with sedimentary-volcanic sequences that host numerous skarn and hydrothermal ore deposits [59]; (2) Cenozoic Zheduo granites (13–41 Ma), located near Kangding town, these granites are thought to have formed as a result of strike-slip movement along the fault [60]. Since the XSHF is an intra-block strike-slip fault within the Bayankala block, rather than a suture zone, no ophiolitic or mafic-ultramafic rocks have been identified along its length.

Elevations along the XSHF range from ~3000 m to 7556 m, with a boiling temperature of ~88 °C. The annual average temperature in the area is below 8 °C. The heat flow value is 94.7 mW/m^2, significantly higher than the continental China average of 63 mW/m^2, and the geothermal gradient is approximately 32.69 °C/km [61,62]. Hot springs along the XSHF are distributed from north to south across counties such as Luhuo, Daofu, Bamei, and Kangding. In Kangding, two distinct geothermal systems are located north and south of the county seat: the Yulingong Geothermal System and the Zhonggu Geothermal System, respectively. Previous studies report reservoir temperatures of 100 °C in Luhuo, 125 °C in both Daofu and Bamei, 220 °C in Zhonggu, and 260 °C in Yulingong [39,63].

3. Material and methods

Geothermal samples were collected in October 2017 and October 2022. Out of 25 sampling sites, 9 were geothermal wells with depths ranging from 40 m to 2006 m, while the remaining 16 were hot springs. Photos of the sampling site of XS02, XS04, XS16, and XS17 are shown in Fig. S1. The sampling temperatures varied between 26 °C and 198 °C, and the corresponding elevations ranged from 2614 m to 3944 m. In the field, water temperatures at the sampling points were measured using an infrared thermometer, and the pH values of the geothermal water were determined with handheld meters that had been calibrated prior to sampling. Raw water samples for stable water isotope analysis (^2H and ^{18}O) were stored in 20 ml polyethylene bottles without the addition of chemical agents. Gas samples were collected from bubbling hot springs using Teflon funnels and from geothermal wells using wellhead water-steam separators, as detailed in Arnórsson et al. [64] and Tian et al. [39]. Three parallel gas samples for composition analysis, stable carbon isotopes, and stable noble gas isotopes were gathered in 50 mL lead glass containers using the gas drainage method, a straightforward collection technique documented in the literature [65]. To minimize the risk of diffusion and atmospheric contamination during transport, we enhanced the storage method as follows: approximately 15 mL of hot spring water was left in the glass bottle before sealing it with a butyl rubber stopper. The glass bottle was then encapsulated upside down in a 500 mL brown polyethylene bottle filled with in-situ geothermal water. This approach reduces the concentration gradient between the inside and outside of the glass bottle, thereby limiting diffusion. Samples for hydrogen isotope determination were collected using a Giggenbach bottle [66] to absorb acidic gaseous components, such as CO_2, H_2S, on-site (Fig. 2).

All samples were analyzed within one month after the field trip. The Oxygen and hydrogen isotopes of water were measured using a laser absorption water isotope spectrometer (L1102-I, Picarro) at the Water Isotope and Water-Rock Interaction Laboratory, Institute of Geology and Geophysics, Chinese Academy of Sciences. The isotopic ratios of D/H and $^{18}O/^{16}O$ are reported to the VSMOW (Vienna Standard Mean Ocean Water) international standard. The analytical precision for δ^2H and $\delta^{18}O$ measurements was 0.5 ‰ and 0.1 ‰, respectively. Gas samples were analyzed at the Key Laboratory of Petroleum Resources Research, Northwest Institute of Eco-Environment and Resources, Chinese Academy of Sciences. These samples were tested for H_2, N_2, CH_4, CO, H_2S, CO_2, C_2H_4, C_2H_6, and C_3H_8 using gas chromatography (GC-9560-PDD) with helium as the carrier gas. O_2 and Ar concentrations were determined with a MAT 271 mass spectrometer. The detection limit was 0.0001 %, with an analytical precision of 0.001 % and relative standard deviations below 5 %. Trace helium content, along with $^3He/^4He$ and $^4He/^{20}Ne$ ratios, was analyzed using a Noblesse noble gas mass spectrometer (Nu Instruments, UK). The detection limit for helium was 0.0001 %, with isotopic ratio measurement errors of less than 7 %. Air collected from Gaolan Hill, south of Lanzhou, was used to calibrate the instrument. The $\delta^{13}C_{V\text{-}PDB}$ values for CO_2 and CH_4 (relative to the VPDB standard) were measured using a GC-IRMS analytical system, comprising a gas chromatography (Agilent 6890) coupled with a Thermo-Fisher Scientific Delta Plus XP stable isotope ratio mass spectrometer and an online sample preprocessor. The carbon isotope ratios are reported using the conventional delta notation (‰) relative to the Pee Dee Belemnite (PDB) standard from South Carolina, with a measurement error of ±0.2 ‰. The D/H ratios of methane and hydrogen were analyzed with a MAT 253 mass spectrometer (Thermo Fischer). A working standard gas (CH_4) with a known hydrogen isotopic composition ($\delta D_{vsmow} = -146.0$ ‰) was used to monitor the instrument's stability and accuracy during each test. Measurement errors for hydrogen isotopic ratios were within ±5 ‰.

4. Results

The gaseous components are listed in Table 1. With the exception of samples XS14 and XS18, CO_2 was the predominant gas in the hydrothermal springs, comprising over 80 % by volume, consistent with typical observations across the Tibetan Plateau [25,33,67]. Minor components included N_2, O_2, Ar, CH_4, H_2, He. Most samples had N_2/Ar ratios ranging from approximately 38 (the value of air-saturated water, ASW) to 83.6 (the value for pure air). In the N_2-He-Ar ternary diagram (Fig. 3a), the data points generally followed a mixing trend between deep-sourced (mantle/crustal) gases and air-contaminated endmembers, indicating that the N_2 and Ar were primarily of atmospheric origin. The concentrations of H_2 and CH_4 ranged from 0.0005 % to 1.69 % and 0.01 %–3.97 %, respectively, corresponding to a broad H_2/CH_4 ratio range of 0.0005–2.59, spanning six orders of magnitude. Helium (He) concentrations varied between 0.0004 % and 0.0725 %. All samples showed O_2 concentrations below 5 % and Ar levels below 0.2 %, suggesting minimal air contamination during sampling [68].

As listed in Table 2, the $^3He/^4He$ ratios ranged from 1.65×10^{-7} to 4.09×10^{-6}, corresponding to R/Ra values of 0.12–2.92 Ra, where Ra represents the $^3He/^4He$ ratio in air (1.43×10^{-6}). The air-corrected $^3He/^4He$ values (reported as Rc/Ra) ranged from 0.11 Ra to 2.90 Ra, falling between the typical crustal value (0.005–0.02 Ra [71]) and mantle values (8 ± 1 Ra for depleted Mid-ocean Ridge Basalts Mantle [72] or 6 ± 2 Ra for subcontinental lithospheric mantle [73]). The $^4He/^{20}Ne$ ratios (0.98–178) were 3–560 times higher than those of the air (0.318) and air-saturated water (~0.26 at 10 °C) [74], suggesting minimal air contamination in the helium samples. The

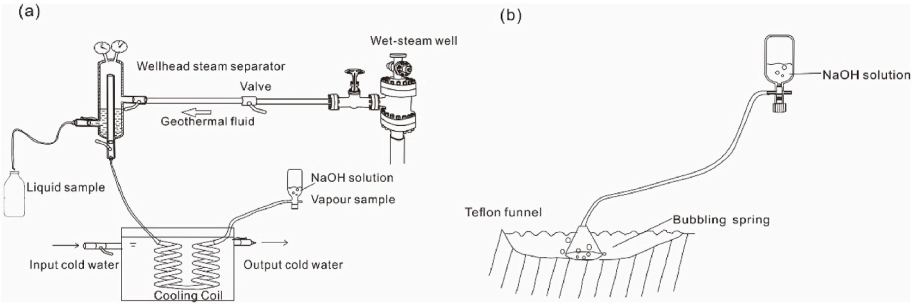

Fig. 2. Sampling methods using the Giggenbach bottle at (a) geothermal wells and (b) bubbling springs, respectively.

Table 1
Information of sampling sites and chemical compositions of geothermal gas.

No.	Area	Type[a]	Sampling Temperature (°C)	Elevation (m)	pH	Gas concentration						
						He (ppmv)	H_2 (vol. %)	O_2 (vol. %)	Ar (vol. %)	N_2 (vol. %)	CH_4 (vol. %)	CO_2 (vol. %)
XS01	Kangding	hs	74	2957	8.1	10	0.0056	3.75	0.18	14.65	0.17	81.24
XS02	Yulingong	gw (2006)	198	3065	9.3	9	0.2756	1.94	0.10	8.51	0.11	89.06
XS03		gw (267)	150	3065	9.0	12	0.6608	0.42	0.02	1.94	0.44	96.51
XS04		hs	70	3012	7.4	15	0.2929	1.41	0.07	5.93	0.40	91.90
XS05		gw (248)	80	3150	7.2	13	1.6900	0.36	0.04	2.98	0.88	94.06
XS06		gw (220)	149	2928	9.5	34	0.3800	0.11	0.02	1.94	0.35	97.19
XS07	Kangding	gw (40)	57	3214	7.2	115	0.0032	1.53	0.57	31.36	3.97	62.55
XS08	Zhonggu	gw (50)	65	3124	7.3	14	0.0039	0.95	0.07	4.11	0.63	94.23
XS09		gw (40)	46	2614	6.9	15	0.0014	0.40	0.03	6.66	0.13	92.77
XS10		gw (1847)	84	3117	7.9	42	1.5400	1.70	0.13	10.84	3.53	82.25
XS11		gw (70)	70	3032	8.1	534	0.0035	1.24	0.11	8.93	0.16	89.53
XS12	Bamei	hs	71	3423	8.6	103	0.0020	1.36	0.25	16.67	2.03	79.68
XS13		hs	26	3630	6.8	68	0.0045	1.00	0.16	10.74	1.23	86.86
XS14	Daofu	hs	53	3944	7.3	725	0.0090	0.85	1.65	61.04	1.88	34.49
XS15		hs	40	3672	7.4	33	0.0168	3.31	0.20	15.31	0.16	81.00
XS16	Luhuo	hs	39	3401	7.2	4	0.0050	1.16	0.06	3.53	0.01	95.23
XS17		hs	35	3055	7.2	–	0.0005	0.13	0.09	7.84	0.16	91.78

[a] hs represent hot spring, gw represent geothermal well with the depth indicated in parentheses.

three-end-member mixing diagram (Fig. 3b) illustrates the relative contributions of mantle, crustal, and atmospheric helium sources. In most samples, the mantle-derived helium content was below 5 %, indicating that helium in the study area primarily originates from the α decay of radioactive elements (U and Th) within the crust. This finding aligns with previous studies from the Tibetan Plateau [31,75], where mantle volatiles have been significantly diluted within the thickened crust (over 60 km). However, the mantle contribution in the Kangding geothermal field (Yulingong and Zhonggu) was notably higher, ranging from 10 % to 30 %, compared to other geothermal systems along the XSHF. Previous studies suggest that this elevated mantle contribution results from a well-developed fracture system that channels mantle volatiles upward in the Moho-uplifted area, rather than from a shallow mantle magma chamber [39]. Indeed, the R/Ra values of Kangding geothermal systems (0.36–2.86 Ra) were considerably lower than those of the Tengchong volcanic field (R/Ra = 5.27) in the southeastern Tibetan Plateau [67]. The isotopic compositions of water samples ranged from δD_{H2O} values of −144.8 ‰ to −114.4 ‰ and $\delta^{18}O$-H_2O values of −18.3 ‰ to −14.0 ‰. According to previous studies [39,63] and as shown in Fig. 3c, the hydrothermal water originated from meteoric sources, with samples from Yulingong displaying a $\delta^{18}O$ shift due to intensified regional water-rock interactions. Other isotopic compositions in the samples were as follows: $\delta^{13}C_{CO2}$ from −7.5 ‰ to −4.8 ‰, $\delta^{13}C_{CH4}$ from −60.7 ‰ to −2.0 ‰, δD_{CH4} from −242.1 ‰ to −31.8 ‰, δD_{H2} from −655.7 ‰ to −507.7 ‰. The δD values of methane and hydrogen were compared with the δD_{H2O} values and sampling elevation, as shown in Fig. 4. The δD of hydrogen exhibits a more significant positive correlation with both the δD value of water and elevation. Additionally, the pH values of the hot spring water varied from 6.8 to 9.5. The implications of these values will be discussed in the following section.

5. Discussion

5.1. He-CO_2 systematics and CO_2 provenance

It is well established that the mantle, carbonate rocks, and organic sediments contribute to the total carbon inventory, with distinct $\delta^{13}C$ values of −6 ± 2.5 ‰, 0 ± 2 ‰, and −30 ± 10 ‰, respectively [65]. In our samples, $\delta^{13}C_{CO2}$ values range from −8.5 ‰ to −2.5 ‰, with an average value of −5.9 ‰. However, pinpointing the exact sources using carbon isotopic data alone is challenging because carbon from the mixing of metamorphic carbonate and sedimentary products can exhibit $\delta^{13}C$ values similar to those of mantle-derived carbon. As the dominant component, CO_2 acts as a carrier gas for other geothermal volatiles, such as He, H_2, and CH_4, during its ascent from deep within the Earth. Relationships between CO_2 and He are commonly used to quantify carbon sources [76] although they are not always tightly coupled during fluid migration [77]. Processes such as hydrothermal degassing and calcite precipitation can cause elemental and isotopic fractionation within the CO_2-He systematics [78].

The $CO_2/^3He$ ratios in our samples range from 1.4×10^9 to 2.8×10^{11}, encompassing values between the mantle (~2×10^9) and crustal ranges (1×10^{11} to 1×10^{13}) [76]. As illustrated in Fig. 5a, most

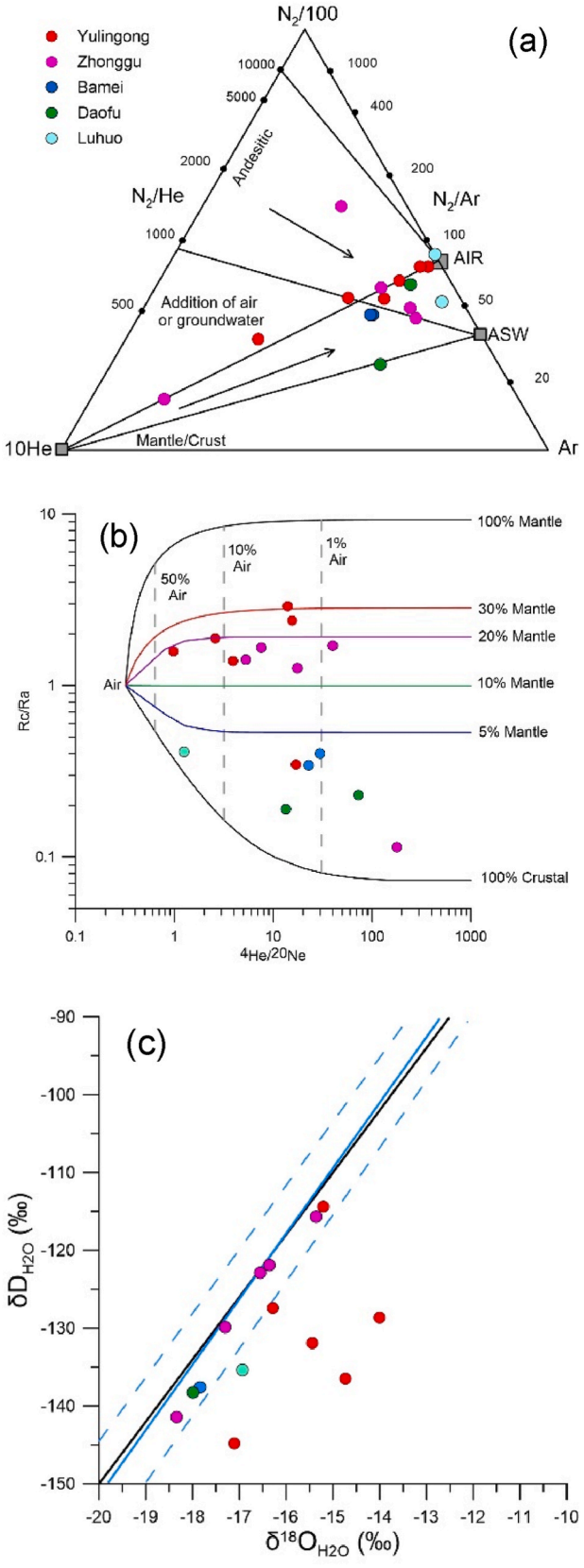

Fig. 3. Plot of (a) N_2-He-Ar; (b) He/Ne ratios versus the Rc/Ra ratios, where the mixing-boundary lines are built from the method proposed by Sano and Wakita [69]; (c) δ^2H_{H2O} versus $\delta^{18}O_{H2O}$, the black solid line represents the global meteoric water line (GMWL: $\delta^2H = 8\delta^{18}O+10$), the blue solid and dashed lines represent the regional meteoric water line with confidence interval for the Tibetan Plateau domain $\delta^2H=(8.41 \pm 0.20)\delta^{18}O+(16.72 \pm 2.98)$ [70].

samples, except for XS07 from Zhonggu and XS14 from Daofu, fall within the triangular domain defined by mantle volatiles, crustal gases, and additional CO_2 sources. Samples from Zhonggu and Yulingong show clear contributions from mantle volatiles, while other samples with $CO_2/^3He$ ratios exceeding 10^{10} indicate a predominantly crustal origin. Using the ternary hybrid model [65], we estimated the contributions from the mantle, carbonate rocks, and metamorphic sediments (Table 2, Fig. 5b). In most cases, crustal metamorphic products accounted for over 90 % of the carbon inventory, with carbonate rocks contributing approximately 70–80 % and organic sediments contributing 10–20 %. However, XS04 and XS05 from Yulingong showed relatively high mantle contributions (~8.5 %), with Rc/Ra values reaching 2.9 Ra. Notably, XS07, XS10, and XS11 from Zhonggu, along with XS12 from Bamei and XS14 from Daofu, exhibited mantle-derived CO_2 fractions exceeding 10 %, with some samples reaching up to 100 % (Table 2). Given their relatively low CO_2 contents (34.5–89.5 %) and depleted $\delta^{13}C$ values, secondary CO_2 loss processes may have masked the primordial contribution by decoupling the He-CO_2 system.

Low CO_2 contents can result from both air contamination and calcite precipitation. However, the N_2/O_2 ratios for XS07 and XS14 were 20.5 and 71.7, respectively, significantly higher than the air value of 3.7, indicating minimal air contamination in these samples. Thermodynamically, mineral solubility varies with temperature and pressure, and calcite precipitation often occurs during the early stages of boiling and degassing [79]. During degassing, CO_2 can be sequestered as calcite, which reduces $CO_2/^3He$ ratios and enriches the residual gases with more negative $\delta^{13}C$ values. Following [80], the $\delta^{13}C$ value of residual CO_2 can be calculated under the assumption that calcite precipitation was in isotopic equilibrium in an open system subject to Rayleigh fractionation [81]:

$$\delta^{13}CO_{2f} = \left(\delta^{13}CO_{2_i} + 1000\right)\left(F^{\alpha_{CO_2-calcite}-1}\right) - 1000 \quad (1)$$

where F is the fraction of remaining CO_2, $\delta^{13}CO_{2f}$ is the carbon isotopic composition of CO_2 at F, $\delta^{13}CO_{2_i}$ is the initial isotope composition of the CO_2, and $\alpha_{CO2\text{-}calcite}$ is the fractionation factor between CO_2 and calcite at a given temperature. The fractionation factor $\alpha_{CO2\text{-}calcite}$ can be estimated using the following equation:

$$1000 \times ln\,\alpha_{CO_2-calcite} = -8.91 \times 10^8 T^{-3} + 8.557 \times 10^6 T^{-2} - 1.881 \times 10^4 T^{-1} + 8.27 \quad (2)$$

where T is the temperature in Kelvin [82]. Since most of the CO_2 emitted from the XSHF is identified as a crustal metamorphic product, the sample with the most negative $\delta^{13}C$ value is considered a result of crustal metamorphism, while the sample with the highest $\delta^{13}C$ value serves as the starting point for isotopic fractionation. Samples XS08 and XS15 were selected as initial points for calcite precipitation in the Zhonggu and Daofu geothermal areas, respectively. As shown in Fig. 5c, the depleted $\delta^{13}C$ value and CO_2 loss in XS07 can be attributed to calcite precipitation occurring at approximately 110 °C, which left less than 70 % of the CO_2 in the gas phase at Zhonggu. Similarly, calcite precipitation at approximately 98 °C resulted in only about 40 % of the CO_2 remaining in XS14 from Daofu. Such degassing processes are plausible, as the reservoir temperatures in Zhonggu and Daofu reach 220 °C [63] and 125 °C [39], respectively, while the actual sampling temperatures in this study ranged between 40 °C and 84 °C.

Based on the calculations above, the degassing of CO_2 in the study area is primarily of crustal origin, with relatively higher contributions from mantle-derived volatiles occurring in the Yulingong and Zhonggu geothermal areas. Given the geological context, Triassic and Paleozoic sedimentary rocks, particularly limestone and sandstone (Fig. 1c), likely serve as the crustal carbon sources. Furthermore, the intense tectonic movements along the eastern margin of the Tibetan Plateau led to stress concentration and an increase in geothermal temperatures, both of which may accelerate chemical reactions within geofluids, such as

Table 2
Isotopic composition and corresponding calculation results of He, Ne and carbon in geothermal gas.

No.	$^3He/^4He$	$^4He/^{20}Ne$	R/Ra	Rc/Ra[a]	$CO_2/^3He$	$\delta^{13}C_{CO2}$	$\delta^{13}C_{CH4}$	CO_2 inventory (%)		
								Mantle	Sediment	Carbonate
XS01	2.53E-06	2.6	1.77	1.88	3.4 E+10	−6.2	−23.0	4.5	19.7	75.8
XS02	1.99E-06	0.98	1.39	1.58	5.1 E+10	−6.9	−22.9	2.9	22.4	74.7
XS03	1.94E-06	3.9	1.35	1.38	4.1 E+10	−5.7	−21.8	3.7	18.0	78.3
XS04	3.38E-06	15.6	2.36	2.39	1.8 E+10	−4.9	−21.4	8.5	14.5	77.0
XS05	4.09E-06	14	2.86	2.90	1.8 E+10	−5.9	−23.7	8.5	17.8	73.7
XS06	5.13E-07	17	0.36	0.35	5.6 E+10	−5.2	−22.9	2.7	16.8	80.6
XS07	1.80E-06	18	1.26	1.26	3.0 E+09	−5.5	−17.0	49.4	7.5	43.1
XS08	1.99E-06	5.3	1.39	1.41	3.4 E+10	−4.8	−21.0	4.4	15.1	80.6
XS09	2.33E-06	7.6	1.63	1.66	2.6 E+10	−5.7	−2.0	5.8	17.6	76.6
XS10	2.43E-06	40	1.70	1.70	8.1 E+09	−7	−23.5	18.6	19.3	62.1
XS11	1.65E-07	178	0.12	0.11	1.0 E+10	−7.1	−22.3	14.7	20.5	64.8
XS12	5.82E-07	30	0.41	0.40	1.3 E+10	−4.8	−19.7	11.3	13.4	75.3
XS13	5.02E-07	23	0.35	0.34	2.5 E+10	−4.8	−19.8	5.9	14.8	79.3
XS14	3.33E-07	73	0.23	0.23	1.4 E+09	−7.4	−13.9	104.9	2.0	−6.9
XS15	2.99E-07	14	0.21	0.19	8.1 E+10	−5.5	−16.5	1.8	18.0	80.1
XS16	8.00E-07	1.3	0.56	0.41	2.8 E+11	−4.9	–	0.5	16.3	83.2
XS17	–	–	–	–	–	−5.1	−60.7	–	–	–

[a] Rc/Ra is the air-corrected He isotope ratio = [(R/Ra)X-1]/(X-1), where X is the air-normalized respective ratio: $X=(^4He/^{20}Ne)_{measured}/(^4He/^{20}Ne)_{air}$. Air: (R/Ra = 1, $^4He/^{20}Ne = 0.318$) [69].

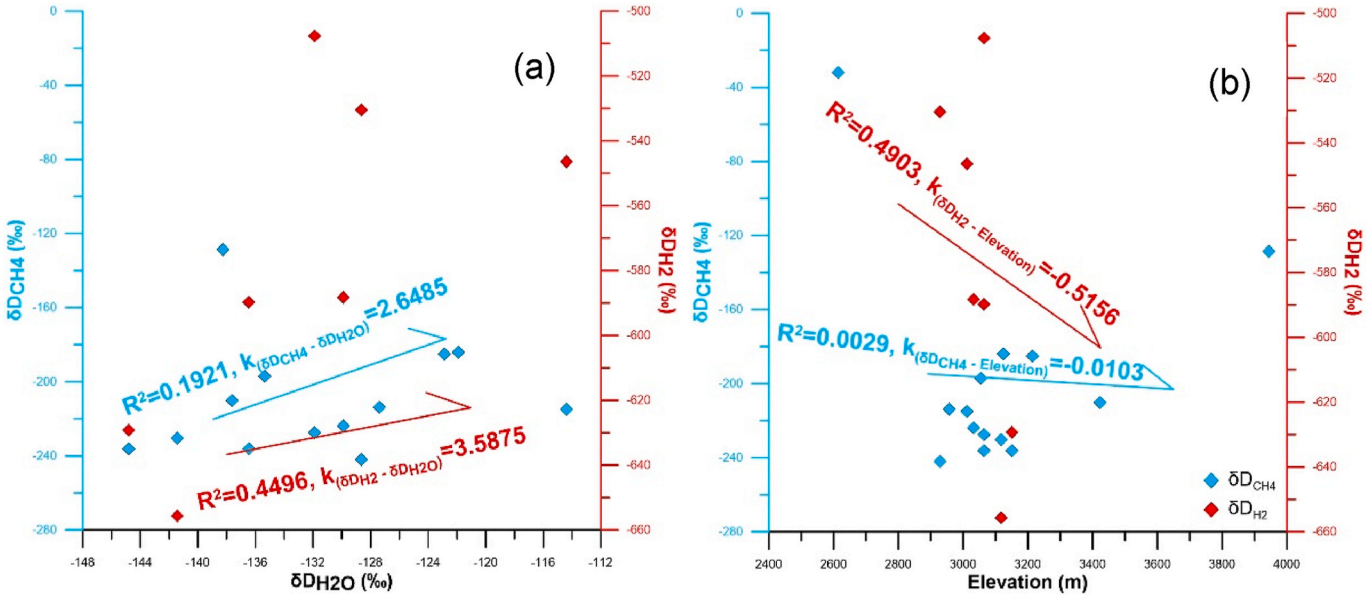

Fig. 4. Plot of δ^2D_{CH4} and δ^2D_{H2} values versus δ^2D_{H2O} value (a) and elevation (b). The R^2 and k values represent the coefficient and the slope of the fit lines, respectively.

hydrolysis, pyrolysis, skarnization of marine carbonates, and dissolution of shallow carbonate minerals. These processes lead to carbonate metamorphism and the release of significant amounts of abiotic CO_2 [83,84]. Additionally, the thermal degradation of organic matter from marine faunal extinction (e.g., plankton sediment) may contribute minor amounts of biotic CO_2 [85,86].

5.2. Origin and isotopic composition of H_2

Hydrogen has been detected in various environments [87]. Its measurable concentration indicates that the source must be geologically young, as H_2 molecule is highly reactive and mobile. As summarized by Zgonnik [24], the main processes contributing to hydrogen generation on Earth include: (1) Degassing of hydrogen from the Earth's core and mantle; (2) Water interaction with reducing agents in the mantle (e.g., Al_4C_3, Fe_3C); (3) Serpentinization: the reaction of water with mafic or ultramafic rocks; (4) Contact of water with freshly exposed rock surface; (5) Decomposition of hydroxyls within the mineral lattice structure; (6) Natural radiolysis of water by radioactive decay; (7) Decomposition of organic matter in petroleum depositions and coal basins; (8) Biological activity; (9) Anthropogenic activity. In our study area, mantle-related and anthropogenic processes can be excluded due to the sparsely populated Tibetan Plateau and limited industrial development. Additionally, the absence of oil or gas reservoirs rules out hydrogen production through thermal cracking of organic matter in hydrocarbon reservoirs. Microbial activity is similarly improbable, as hydrogen generation via dark fermentation occurs under mesophilic (25–40 °C), thermophilic (40–65 °C), and hyper-thermophilic (below 80 °C) conditions [88], and the highest temperature at which any organism is known to grow is 121 °C [89]. Whereas reservoir temperatures along the XSHF range from 100 °C to 220 °C. In addition, as a part of the non-volcanic geothermal belt [90], the lithology in the area primarily consists of terrigenous deposits and acidic granitoids. No correlation has been observed between the locations of hot springs and ophiolitic or other mafic rocks (Fig. 1c), suggesting that serpentinization is unlikely to be a significant source of hydrogen.

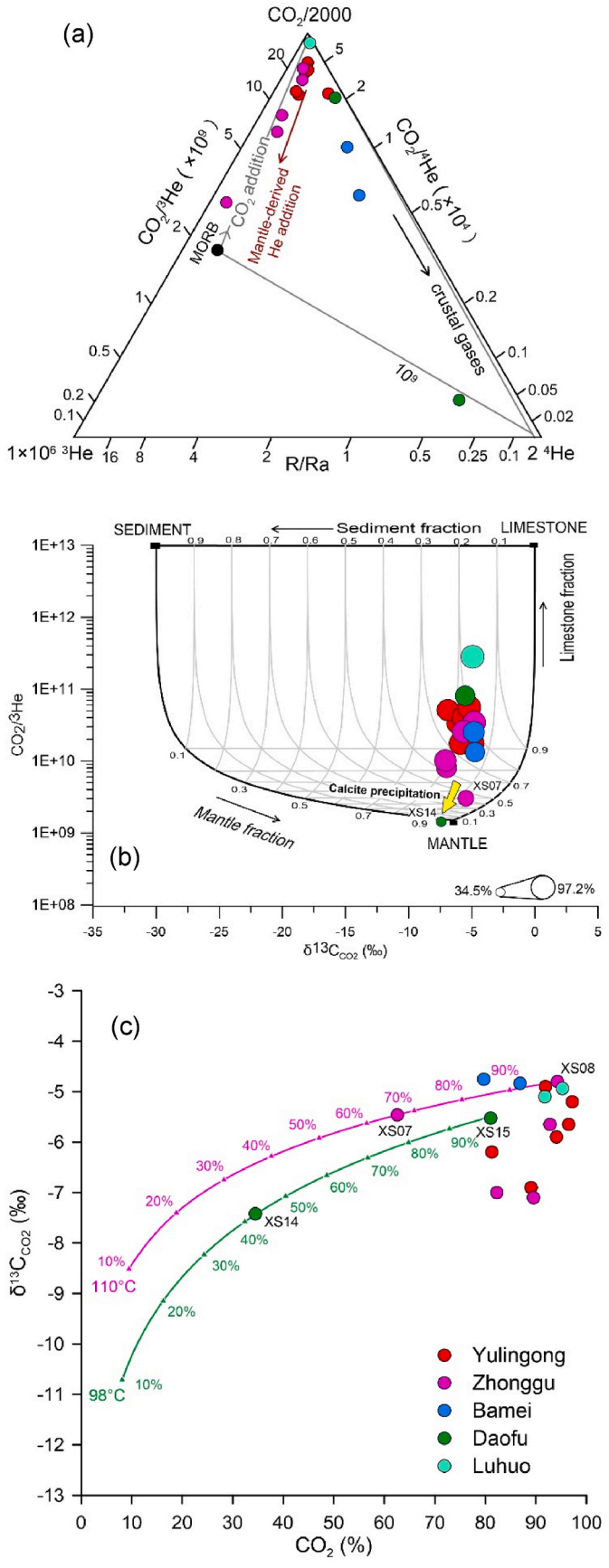

(caption on next column)

Fig. 5. (a) Triangle plot of CO_2-^{3}He-^{4}He; (b) $CO_2/^3$He-$\delta^{13}C_{CO2}$ bubble plot where the increasing radius of bubble indicates the growing CO_2 content. Solid black and grey lines represent the binary mixtures between the different end-member values. Grey dashed lines with triangles show predicted calcite fractionation model [80] trends for CO_2 loss by calcite precipitation at 100 °C (as % lost carbon), assuming a mantle starting composition of $\delta^{13}C = -6.5$ ‰ and $CO_2/^3He = 2 \times 10^9$; (c) Plot of $\delta^{13}C_{CO2}$ values versus CO_2 contents. The pink and green solid lines labeled 110 °C and 98 °C represent isotopic and elemental fractionation of carbon during calcite precipitation from an initial condition represented by the samples of XS08 and XS15, respectively. The triangles are labeled with the fraction of remaining CO_2.

It is important to emphasize that the mantle contribution in the Kangding geothermal field is notably higher than in other geothermal systems along the XSHF, owing to the deeper fault development. This could suggest that mantle-derived H_2 contribute to the elevated H_2 concentrations. However, considering the unique tectonic context of the study area, this scenario is highly improbable. Our data show that two points with high H_2 concentrations in Kangding correspond to high R/Ra ratios, but the correlation across all samples (Tables 1 and 2) is weak, making it difficult to conclusively associate high H_2 concentrations with ^{3}He. While magmatic gases typically have higher H_2 content, as Day and Shepherd [91] reported for lava volatiles in Hawaii's Halemaumau, with H_2 percentages ranging from 6.7 % to 10.2 %, it is noteworthy that the CO content in these gases ranges from 3.5 % to 5.6 %, comparable to the H_2 content. This indicates that the strongly reducing environment of lava favors the preservation of both CO and H_2. In contrast, reports of CO content in geothermal gases from our study area, and from the Tibetan Plateau in general, are rare. While testing limitations may partly explain this, it also highlights the generally low CO concentration. This suggests that even if mantle-derived H_2 and CO were initially dissolved in geothermal fluids, they would likely have undergone oxidation before reaching the surface, depleting much of the CO. Furthermore, the preservation of strongly reducing H_2 in the high-temperature, high-pressure tectonic conditions of the Tibetan Plateau orogenic belt is unlikely, as it would be challenging to maintain and transport it from the ~60 km thick crust to the surface. Our recent study [92] further supports this, showing that the spatial distribution of R/Ra ratios and H_2 concentrations in geothermal gases across the Tibetan Plateau does not exhibit a positively correlated co-variation.

The presence of young Cenozoic Zheduo granite in the Kangding area increases the competitiveness of water-splitting processes related to granite radioactive decay compared to other mechanisms. While this mechanism may contribute to the enrichment of H_2 in the Kangding area, we argue that it is not the dominant factor. The Zheduo-Gongga massif in Kangding has an average uranium (U) content of 7.64 ppm, with a maximum of 12.55 ppm, and an average thorium (Th) content of 43.93 ppm, with a maximum of 55 ppm [93]. These concentrations are significantly higher than the average U (2.5 ppm) and Th (10.33 ppm) concentrations in the upper continental crust [94], indicating that the granites in this region have relatively high radioactivity. Lin et al. [95] estimated the rate of hydrogen production via water-splitting induced by radiolytic decay based on U and Th concentrations in rocks. Using U at 10 ppm and Th at 30 ppm, close to the average concentrations in our study area, they calculated a radiolytic H_2 yield rate of 9.0×10^{-8} nM/s. Assuming a system volume of 1 L, the time required to reach a hydrogen concentration of 0.5 % would be approximately 17,650 years, and to reach 1.69 %, about 5.96×10^6 years. Despite the uncertainties in this rough estimate, such a long accumulation period is clearly inconsistent with the conditions of the XSHF, which is characterized by intense seismic activity and prominent strike-slip faulting.

At last, the distribution of geothermal systems closely follows tectonic lines, with all hot springs occurring at fault intersections, indicating that large-scale faults likely play a key role in determining the chemical composition of geothermal fluids. Therefore, further research into water-rock interactions and mineral decomposition is needed to

better understand these processes. Indeed, hydrogen gas can be generated through both chemical and mechanical changes in rocks. During fault movement, the destruction of basement rock and pulverization of fragments create fresh, highly chemically active surfaces. One mechanism for hydrogen production involves the hydrolysis of silicon (Si·) and silanol (*Si*-O·) groups formed on these fresh surfaces when the *Si*-O-Si bonds between SiO_4 tetrahedra in silicate minerals are disrupted by crushing at depth. This reaction is illustrated in Eq. (3) [96]. Additionally, hydrogen can be released during the decomposition of hydroxyl groups within the lattice structure of minerals at high pressure and temperature (400–600 °C). Under these conditions, hydroxyl pairs, such as O_3Si-OH, can dissociate to release hydrogen (Eq. (4)) [97]. Such fault-related reactions were first identified during earthquake faulting in Japan [98,99] and the United States [100,101]. In China, hydrothermal hydrogen concentrations were found to increase along the Longmenshan Fault (LMSF) following the 2008 Wenchuan Ms 8.0 earthquake [102]. Laboratory studies have confirmed that various rock lithologies, including basalt and granite, can produce hydrogen [103,104]. Given that the decomposition of hydroxyls requires higher temperatures (>400 °C), hydrolysis of silicates is likely the primary mechanism for hydrogen formation. This is further supported by positive correlations between hydrogen concentrations and δD values of our samples with factors such as the strike-slip rate, Rc/Ra values, reservoir temperatures, shallow aseismic slip rate, locking depth, and seismic activities along the XSHF. These factors indicate two essential features necessary for hydrogen accumulation:

$$2(\equiv Si\cdot) + 2H_2O \rightarrow 2(\equiv SiOH) + H_2 \quad (3)$$

$$O_3Si - OH\ HO - SiO_3 \rightarrow O_3Si - OO - SiO_3 + H_2 \quad (4)$$

(1) Hydrothermal reservoirs in deep faults. Although hydrogen was detected in all hot springs, only trace amounts were found in most samples. Concentrations in low-temperature hot springs (Table 1), such as Bamei, Daofu, and Luhuo, were below 0.01 volumetric percent, rendering their isotopic compositions untestable, even with the Giggenbach bottle for absorbing acidic gaseous components on-site. In contrast, hydrogen concentrations in Yulingong and Zhonggu were sufficiently high for isotopic testing. Yulingong is recognized as a representative deep-fault-controlled geothermal field with a reservoir temperature of 260 °C, while Zhonggu has a reservoir temperature of 220 °C [39,63]. The increasing hydrogen content corresponds to the well-developed deep fractures that facilitate groundwater infiltration and heat absorption from surrounding rocks. Additionally, strong isotopic signals of mantle-derived helium (Fig. 6c), high reservoir temperatures (Fig. 6d), and deep locking depths (Fig. 6f) toward the southeast provide compelling evidence for the presence of a deep-extended fracture system.

(2) Strong crustal deformation and intense faulting activity. The XSHF is one of the most tectonically and seismically active faults globally, characterized by varying left-lateral strike-slip rates across its segments [105]. Late Quaternary slip rates along the XSHF progressively increase from northwest to southeast, with averages reaching 9.6–13.4 mm/yr at the southeastern end (Fig. 6a) [49]. Present-day deformation features widespread shallow creep along the fault, with tectonic loading rates of 8.8–17.9 mm/yr and shallow aseismic slip rates of 3.3–19.8 mm/yr (Fig. 6e) [106]. These differential movements are evidenced by more frequent and stronger earthquakes occurring in the southeast segment of the XSHF (Fig. 6g). Since both the locking depth and the focal depth of most earthquakes are less than 20 km, and the brittle/ductile transition depth is reported to be about 20 km [56,107], H_2 is primarily produced at depths shallower than 20 km within fault zones, where fresh mineral surfaces are generated through the brittle fracture of rocks.

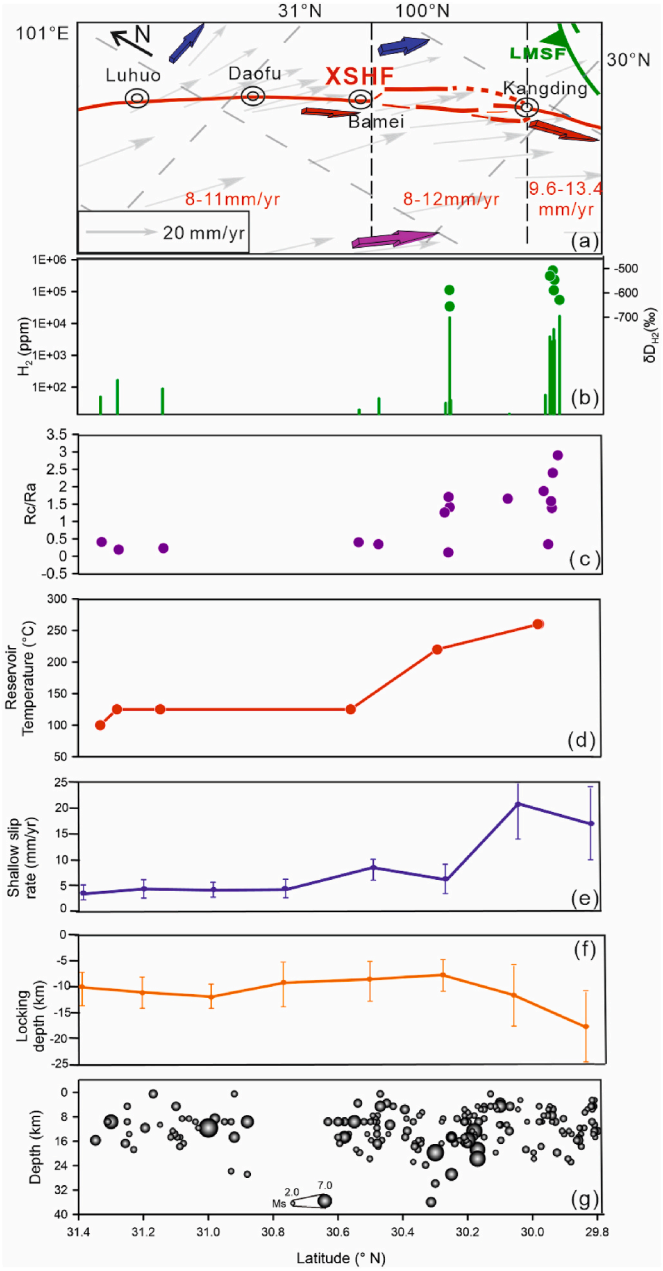

Fig. 6. (a) Summary of fault trace for each segment of the XSHF with best constrained late Quaternary slip rates in red at bottom of figure (modified from Ref. [49]). Red arrows show southeastward slip rate increase. Grey arrows show GPS vectors relative to stable Eurasia [108]. Blue and purple 3D arrows show block movement on each side of the XSHF with their appropriate length according to GPS velocities. The (b) H_2 concentrations (represented by green bars), δD_{H2} values (represented by green dots) and (c) Rc/Ra values of the samples in this study. (d) The reservoir temperatures at Luhuo, Daofu, Bamei, Zhonggu, and Yulingong estimated by Tian et al. [39]. Spatial variations in (e) shallow aseismic slip rate and (f) locking depth inverted from Interferometric Synthetic Aperture Radar (InSAR) data [106]. (f) The focal depths of historical earthquakes with the increasing radius of bubbles represents the increase of earthquake magnitude, detailed information listed in Table S1.

The isotopic composition of hydrogen can provide valuable insights into its source. As initially proposed by Kita [109], δD_{H2} values ranging from −770 ‰ to −470 ‰ indicate that molecular hydrogen is generated through chemical reactions between groundwater and fresh surfaces in fractured basement rocks. In our samples, the isotopic compositions of hydrogen (δD_{H2}) and the isotope fractionation factors between H_2O and

H_2 (αH_2O-H_2) were measured at −507 ‰ to −656 ‰ and 1.8 to 2.5 (Table 3), respectively. These values not only fall within the crustal-origin ranges identified by Kita [109] but also align with the ranges observed in fault zones compiled by Hao et al. [23], which reported δD_{H2} values from −791 ‰ to −242 ‰ and αH_2O-H_2 values of 1.2–4.4. Another interesting observation is that the δD values of our samples fluctuate in tandem with the δD_{H2O} values (Fig. 4a) and the elevation of the sampling sites (Fig. 4b), while δD_{CH4} vary only slightly. Although the positive correlation of hydrogen isotopes in H_2O and H_2 is largely due to isotopic exchange in geothermal fluids, a small part may also result from water-rock interactions. In other words, the hydrogen atoms in H_2 could originate from water molecules through water-rock interactions during the destruction and pulverization of rock fragments in the active strike-slip fault. In summary, the hydrolysis of silicates in active fault planes is likely the primary mechanism responsible for hydrogen degassing in fault-controlled geothermal systems.

5.3. Origin of CH_4

As a minor component of hydrothermal gas, the origin of methane (CH_4) in the Tibetan Plateau has received limited attention in previous studies. Regarding its genetic mechanisms, methane in hydrothermal volatiles can originate from three primary sources: microbial, thermogenic, and abiotic processes. These sources can be distinguished by specific molecular ratios of alkanes (e.g., the $C_1/(C_2+C_3)$ ratio) and the stable carbon and hydrogen isotopic compositions of CH_4 and CO_2. Genetic diagrams illustrating these processes were first proposed in the 1970s and 1980s [110–112] and have since been revised with new data [5,13,20,113,114]. Despite significant effort, distinguishing between biotic and abiotic CH_4 in hydrothermal fluids remains challenging [115]. The diagrams utilized in this study (Fig. 7) are primarily based on the updates by Milkov and Etiope [114] and have been modified for volcanic hydrothermal and volcanic thermogenic areas in accordance with the work of Fiebig et al. [113] and Reeves and Fiebig [5], respectively.

Microbial CH_4 typically has $\delta^{13}C_{CH4}$ values lower than −50 ‰ [116]. This bacterial methane can be further categorized into two groups based on distinct isotopic compositions: gases produced through microbial CO_2 reduction in marine sediments and gases generated via methyl-type fermentation in continental deposits [111,117]. Bradley and Summons [20] referred to these two genetic categories as “autotrophic” and “heterotrophic,” respectively, highlighting that methane in marine sediments is primarily produced through H_2/CO_2 methanogenesis, while methane in terrestrial environments results from the fermentation of acetate or the consumption of methylated organic compounds. Based on these empirical criteria, the methane from XS17 is recognized as a microbial product, likely formed through CO_2 reduction, as its corresponding data point falls within the CO_2-reduction area in both Fig. 7a and b. However, considering the exposure conditions of the XS17 hot spring, which emerges in the mud along the bank of the Xianshui River (Fig. S1), heterotrophic activity may also play a significant role. The river’s fluctuations bury a substantial number of microorganisms and organic matter in the mud, providing the necessary material for methane generation via methyl-type fermentation.

In contrast, CH_4 in other samples showed enrichment in $\delta^{13}C$, with values ranging from −23.7 ‰ to −2 ‰, exceeding the typical lower limit for abiotic CH_4 (−25 ‰) [12]. However, this methane is identified as thermogenic product based on the following evidence. First, the air-corrected $^3He/^4He$ values ranged from 0.11 Ra to 2.90 Ra, with CH_4 concentrations showing no positive correlation with Rc/Ra values. This lack of correlation suggests that the methane is unlikely to originate from mantle or magmatic sources. Second, the possibility of abiotic methane produced by water-rock interactions, such as Fischer-Tropsch synthesis (FTT) reactions and Sabatier reactions, can be ruled out based on several factors: (1) Abiotic CH_4 is predominantly associated with mafic or ultramafic rock systems, where serpentinization of ophiolites or peridotite massifs generates H_2 [16,20,21,118]. (2) According to the reaction formulas, the FTT reaction requires at least a 2:1 ratio of carbon to hydrogen (Eq. (5)) [119], while the Sabatier reaction (Eq. (6)) [120] and the methanation of dissolved bicarbonate (HCO_3^-) under hydrothermal conditions (Eq. (7)) [121] require a 4:1 ratio.

$$nCO + 2nH_2 = -(CH_2)n- + nH_2O \quad (5)$$

$$CO_2 + 4H_2 \rightarrow CH_4 + 2H_2O \quad (6)$$

$$HCO_3^- + 4H_2 \rightarrow CH_4 + OH^- + 2H_2O \quad (7)$$

To produce more abiotic CH_4, conditions must feature significantly higher H_2/CO_2 ratios [122]. (3) Abiotic methane typically exhibits an H_2/CH_4 ratio >40, while biotic methane falls below this threshold [123]. (4) Abiotic methane production requires catalysts like transition metals, their oxides, or alloys [14,124,125]. Naturally occurring catalysts, such as chromite, and secondary minerals like magnetite (Fe_3O_4) or awaruite (Ni_3Fe), typically arise during olivine hydrolysis [123] and are commonly found in serpentinizing peridotites [1] and oceanic crusts [121]. (5) Abiotic methane formation typically occurs in hyperalkaline fluids with pH values of 10–12 (Ca-OH type waters) ([23] and therein references). In contrast, in our study area, the lithology (consisting of terrestrial sedimentary rock and granite), catalyst minerals, H_2/CO_2 ratios (0–0.019), H_2/CH_4 ratios (0–2.59), and pH values (6.8–9.5) do not meet the necessary conditions for abiotic methane formation. Thirdly, in light of the geological and hydrological context, the methane detected in

Table 3
Isotopic composition and corresponding calculation results of He, Ne and carbon in geothermal gas.

No.	δD_{CH4}	δD_{H2}	δD_{H2O}	$\alpha_{H2O\text{-}H2}$	$\varepsilon_{H2\text{-}H2O}$	$\varepsilon_{CH4\text{-}H2O}$	$\alpha_{CH4\text{-}H2}$	$\alpha_{CO2\text{-}CH4}$	$T\alpha_{H2O\text{-}H2}$ (°C)[a]
XS01	−213.8	–	−127.4	–	–	–	–	1.02	–
XS02	−227.4	−507.7	−131.9	1.8	−567	−117	1.57	1.02	258
XS03	−236.2	−589.8	−136.5	2.1	−744	−123	1.86	1.02	169
XS04	−215.1	−546.4	−114.4	2.0	−669	−121	1.73	1.02	202
XS05	−236.2	−629.2	−144.8	2.3	−836	−113	2.06	1.02	135
XS06	−242.1	−530.5	−128.6	1.9	−618	−140	1.61	1.02	228
XS07	−185.1	–	−122.9	–	–	–	–	1.01	–
XS08	−184.0	–	−121.9	–	–	–	–	1.02	–
XS09	−31.8	–	−115.7	–	–	–	–	1.00	–
XS10	−230.2	−655.7	−141.4	2.5	−914	−109	2.24	1.02	110
XS11	−223.8	−588.2	−129.9	2.1	−748	−114	1.89	1.02	167
XS12	−210.1	–	−137.6	–	–	–	–	1.02	–
XS13	–	–	–	–	–	–	–	1.02	–
XS14	−128.7	–	−138.3	–	–	–	–	1.01	–
XS15	–	–	–	–	–	–	–	1.01	–
XS16	–	–	–	–	–	–	–	1.06	–
XS17	−197.0	–	−135.4	–	–	–	–	–	–

[a] $T\alpha_{H2O\text{-}H2}$ represent the calculated equilibrated temperature according to Eq. (10).

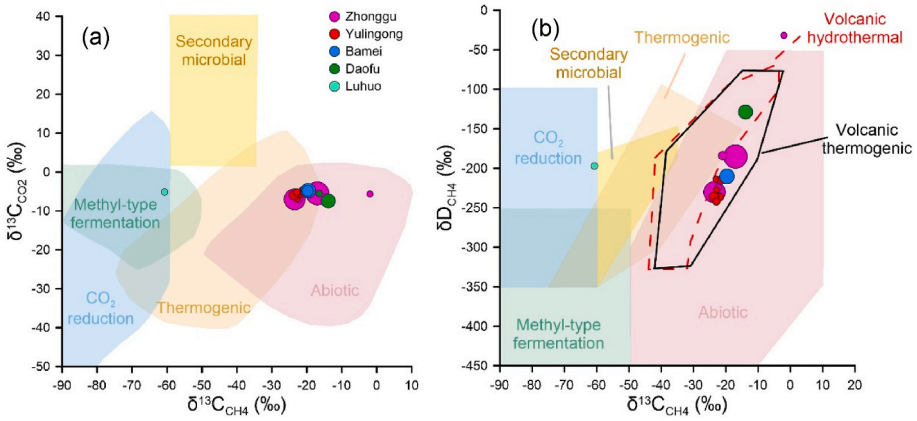

Fig. 7. Methane genetic diagrams based on (a) $\delta^{13}C_{CO2}$ versus $\delta^{13}C_{CH4}$; (b) $\delta^{2}D_{CH4}$ versus $\delta^{13}C_{CH4}$.

most samples is likely of thermogenic origin. As illustrated in Fig. 7, most samples fall within the overlapping region of thermogenic and abiotic fields in the $\delta^{13}C_{CO2}$ versus $\delta^{13}C_{CH4}$ plot (Fig. 7a) and in the transition area between these two systems in the δD_{CH4} versus $\delta^{13}C_{CH4}$ plot (Fig. 7b). Slight enrichments of $\delta^{13}C$ and δD in methane may result from the thermal degradation of organic matter in a high-temperature open system [113], biotic methane formation under carbon-limited conditions [126] or microbial hydrogenolysis of sedimentary organic matter [127]. Among these mechanisms, thermal degradation appears the most plausible due to: (1) the high-temperature geothermal setting, supported by hydrochemical studies [39] and a high terrestrial heat flow of 94.7 mW/m^2 [61]; and (2) the presence of organic matter, as estimated in Section 5.1, where metamorphic products of organic sediments contribute approximately 10–20 % of the total CO_2 carbon inventory. The organic matters may originate from nearby sedimentary rocks or from meteoric water circulating through a high-temperature open system [5]. Additionally, biological consumption of methane by anaerobic and aerobic methanotrophs can lead to coherent enrichment of δD and $\delta^{13}C$ in residual methane [128,129]. This phenomenon could explain the extremely heavy isotopic compositions in samples XS09 and XS14.

Another noteworthy observation is that methane was the only carbon-bearing compound detected besides CO_2, and it was the only hydrocarbon with concentrations (0.01 %–3.53 %) exceeding the detection limit (1 ppm) of the instruments. In contrast, the concentrations of CO, C_2H_4, C_2H_6, and C_3H_8 in the samples were below detection limits. This finding aligns with the lack of data on hydrothermal CO and C_2+ hydrocarbons in Western Sichuan and the Himalayan Geothermal Belt [30,31,40,75,84]. If the methane is indeed a thermogenic product formed during the thermal cracking of kerogen or crude oil in sediments, the expected formation temperatures would range between 157 °C and 221 °C [130]. According to the Bernard plot [131], the ratio of methane concentration to the summed concentrations of higher-chain hydrocarbons (ethane and propane) should vary between 1 and 100. However, C_2+ hydrocarbons remain undetectable even when methane concentrations reach 5 %. Further investigation into these consistently low C_2+ hydrocarbon concentrations could provide additional evidence for the mechanisms behind methane formation.

5.4. H_2-H_2O-CH_4-CO_2 isotope systematics

Comparison of observed and equilibrium fractionations can provide valuable information regarding the fluid evolution in hydrothermal systems [132]. Taken the coexisting H_2O and H_2 as example, the D/H isotope fractionation factor (α) is calculated according to:

$$\alpha_{H_2O-H_2}=\frac{\delta D_{H_2O}+1000}{\delta D_{H_2}+1000} \quad (8)$$

and the enrichment factor (ε) value is defined as $\varepsilon = 1000\ln\alpha$, for example:

$$\varepsilon_{H_2O-H_2}=1000\ ln\ \alpha_{H_2O-H_2} \quad (9)$$

The equilibrium fractionation factors, $\alpha_{H2O\text{-}H2}$ [133], $\alpha_{H2O\text{-}CH4}$, $\alpha_{CH4\text{-}H2}$ [134], and $\alpha_{CO2\text{-}CH4}$ [135], at a given temperature were estimated according to the respective equations:

$$\alpha_{H_2O-H_2}=1.00138+\frac{219,788}{T^2}-\frac{2.926E+09}{T^4}+\frac{4.108E+14}{T^6} \quad (10)$$

$$\alpha_{H_2O-CH_4}=1.0997+\frac{8456}{T^2}+\frac{0.9611E+09}{T^4}-\frac{27.82E+12}{T^6} \quad (11)$$

$$\alpha_{CH_4-H_2}=0.8994+\frac{183,540}{T^2} \quad (12)$$

$$10^3\ ln\ \alpha_{CO_2-CH_4}=0.16+\frac{1.175E+07}{T^2}-\frac{2.366E+09}{T^3}+\frac{2.054E+11}{T^4} \quad (13)$$

where T is absolute temperature (K). The $\alpha_{H2O\text{-}H2}$, $\alpha_{CH4\text{-}H2}$, $\alpha_{CO2\text{-}CH4}$, $\varepsilon_{CH4\text{-}H2O}$, $\varepsilon_{H2\text{-}H2O}$ values and the calculated equilibrated temperatures of our samples are listed in Table 3.

In Fig. 8a, nearly equilibrium fractionation is observed across all samples, indicating that hydrogen exchange equilibria between CH_4-H_2 and H_2O-H_2 were achieved. Specifically, samples from Zhonggu equilibrated at temperatures between 110 and 160 °C, which is lower than the estimated reservoir temperature of 220 °C [39]. Moreover, the sampling temperatures in Zhonggu deviate significantly from the H_2O-H_2 equilibrium temperatures accociated with the corresponding $\alpha_{H2O\text{-}H2}$ values (Fig. 8b). Drawing on current understanding of the study area's hydrological conditions [136], mixing with shallow cold water and quenched isotopic re-equilibration could explain these deviations [133]. In contrast, an interesting observation arises with the deepest drillhole in the Yulingong geothermal system: the equilibrium temperature of XS02 reaches 258 °C, closely matching the reservoir temperature of 260 °C estimated from hydrochemical concentrations [39,63]. This indicates that the hydrogen isotopic correlations between CH_4-H_2 and H_2O-H_2 in XS02 accurately reflect the reservoir fluid conditions. Two factors likely contribute to this phenomenon. First, boiling appears to have minimal effect on isotope fractionation between H_2O and H_2. During adiabatic boiling of hydrothermal fluid from 250 to 300 °C down to 100 °C, the δD difference between vapor and residual liquid would alter the $\alpha_{H2O\text{-}H2}$ value by less than 0.1 [133,137]. Second, the XS02 samples were nearly pure reservoir fluid, quickly brought to the surface through the drillhole. As shown in Fig. 8b, XS02 lies on the kinetic fractionation trend calculated for a 1-min travel time, confirming rapid upflow through the deep drillhole. In other words, XS02 has effectively reached the Yulingong

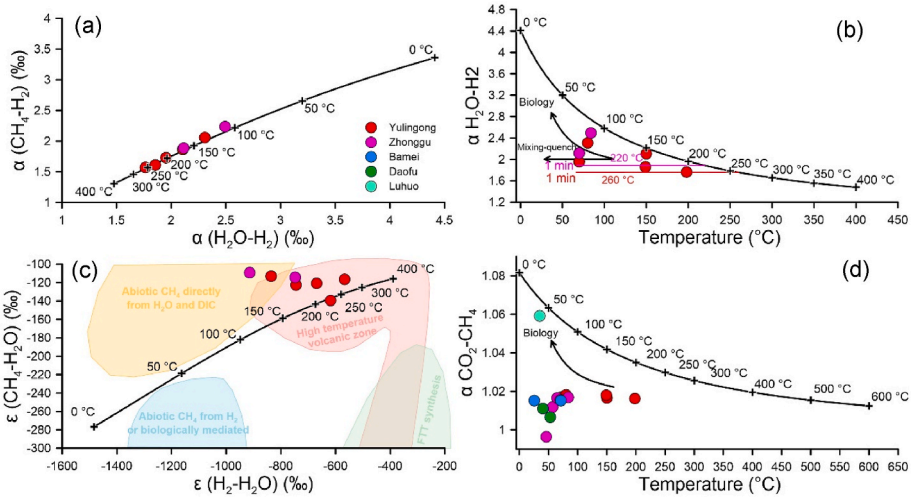

Fig. 8. Hydrogen isotope concordance diagrams showing fractionation in the CH_4-H_2O-H_2 system: (a) $\alpha_{CH4\text{-}H2}$ versus $\alpha_{H2O\text{-}H2}$; (b) $\alpha_{H2O\text{-}H2}$ versus measured sampling temperature. The red and pink lines show the kinetic fractionation trends by solving the kinetic modelling [133,137] for reservoir temperatures of 260 °C and 220 °C with a travel time from reservoir to surface of 1 min; (c) $\varepsilon_{CH4\text{-}H2O}$ versus $\varepsilon_{H2\text{-}H2O}$, the empirical areas modified from Refs. [23,129]; (d) $\alpha_{CO2\text{-}CH4}$ versus measured sampling temperature. The solid line in each diagram shows the equilibrium fractionation at different temperature.

geothermal reservoir at a depth of 2006 m. This finding aligns with multiple hydrochemical and geophysical studies. For example, the water chemical composition approaches full equilibrium on the Na-K-Mg triangular diagram at 260 °C [39,63], as defined by Giggenbach [138], indicating equilibrium with primary reservoir rock minerals, such as albite and microcline. Besides, a magnetotelluric survey by Cheng et al. [139] identified a highly resistive layer at around 2 km depth with a thickness of ~200 m, interpreted as a liquid-dominated reservoir. Together with our previous conclusions, these results suggest that geothermal water in the Yulinggong geothermal system circulated to greater depth, where it was heated to 260 °C before rising and being stored at 2 km depth. This process is driven by intense convective activity in groundwater and heat flow, controlled by Kangding's unique structural conditions, particularly the development of deep faults in a high-temperature setting.

Isotope exchange between CH_4-H_2O and CO_2-CH_4 haven't achieved equilibrium in our samples. As shown in Fig. 8c, except for one from Yulingong, all samples plot above the concordance line of $\varepsilon_{CH4\text{-}H2O}$ and $\varepsilon_{H2\text{-}H2O}$ values, in a linear fashion. This consistent deviation indicates the origin of methane is uniform. Compared with the empirical areas documented in previous studies, methane in this study plot outside of the abiogenic zones, consistent with the conclusion of biotic origins drawn in former sections. Moreover, the thermogenic methane has $\varepsilon_{CH4\text{-}H2O}$ values similar to those obtained for high-temperature volcanic geothermal systems [23], suggesting that simultaneous high values of $\varepsilon_{CH4\text{-}H2O}$ and $\varepsilon_{H2\text{-}H2O}$ can also occur in non-volcanic high-temperature geothermal fluids. In addition, the deviation from the ideal is greater at the lower-temperature area, indicating that the CH_4-H_2O geothermometer yields a higher predicted temperature than does the H_2O-H_2. The reasons for this discordance are likely related to sluggish isotope equilibrium at low temperatures and to biological activity [132]. With regards to carbon isotope, the exchange between CH_4 and CO_2 are far from equilibrium in our samples, except for XS17 exhibit the minimal discrepancy between the theoretical equilibrium temperature (~60 °C) and the measured temperature (35 °C) (Fig. 8c). The enhanced equilibration in XS17 could be facilitated by the micro-organisms which catalyze D-H exchange at temperature lower than 60 °C [20,133]. Indeed, methane from XS17 has been recognized as microbial product in Section 5.3. In contrast, larger deviations in other samples likely stem from unrelated sources and insufficient isotope exchange time. From a source perspective, our earlier discussions have established that there is no genetic relationship among H_2, CH_4, and CO_2. However, from a reaction rate perspective, theoretical estimations can be derived based on the isotopic exchange equilibration in the H_2-H_2O-CH_4-CO_2 system, assuming isotope exchange occurs in aqueous fluids. As shown in Fig. 9, equilibrium between H_2 and H_2O in the liquid phase can be reached within approximately 1.5 h at 260 °C and 3.6 h at 220 °C, enabling rapid exchange under reservoir conditions. However, methane, as the most thermodynamically stable carbon-bearing form [121], has a much slower isotope exchange rate, requiring timescales approaching or even exceeding the age of the Earth at temperatures below 100 °C.

5.5. *Gas evolution and the resource potential of H_2 and CH_4*

Based on the above analysis, we propose a conceptual model for gas evolution in the fault-controlled geothermal system at Kangding

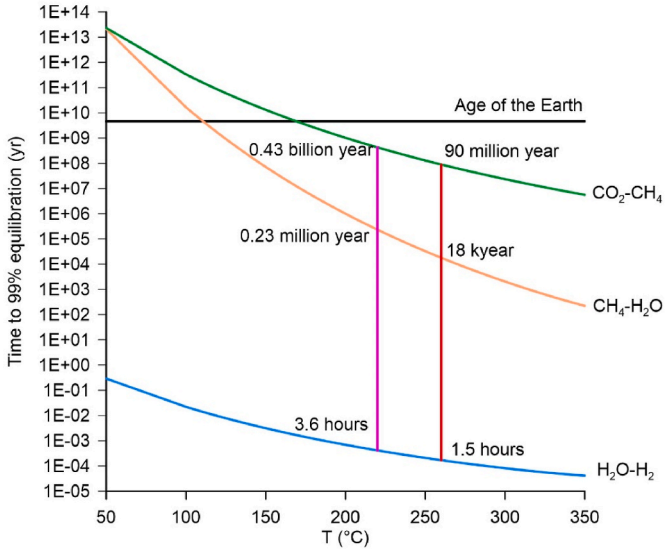

Fig. 9. The calculated time for 99 % fractional equilibration for $^{13}C/^{12}C$ and $^{2}H/^{1}H$ between CO_2, CH_4, H_2O and H_2 as a function of temperature in aqueous liquid. The calculations are based on rate expressions for CH_4-CO_2 (green line) [135], CH_4-H_2O (orange line) [140], and H_2O-H_2 (blue line) [133], which were compiled by Ref. [115]. The black, red and pink lines represent the age of the Earth (4.6 billion years) [141], and the reservoir temperature of 260 °C and 220 °C, respectively.

Yulingong (Fig. 10). The dissolved gases in geothermal water include CO_2, N_2, Ar, He, CH_4, H_2, etc. Among these, the chemically inert gases N_2 and Ar are primarily derived from atmospheric air, which infiltrates underground through precipitation and accumulates as other oxidizing gases are consumed during groundwater circulation. At the same time, gases from deeper sources, such as He, CO_2, H_2 and CH_4, gradually dissolve into the geothermal water. He is mainly produced by the decay of uranium and thorium in the crust, with a notable proportion of primordial ^{3}He introduced at deep fault zones. CO_2 mainly originates from the metamorphism of carbonate rocks and organic matter within the crust, with additional mantle-derived CO_2 mixing in at deep fault zones. Organic matter buried in sedimentary rocks or transported by infiltrating groundwaters undergoes thermal metamorphism at depth, producing not only trace amounts of CO_2 but also a significant quantity of CH_4, which dissolves into the geothermal fluid. In contrast, H_2 is primarily produced along the fracture surfaces of active fault zone, where it forms through mechanoradical processes involving cataclastic silicates in the presence of water. This process is associated with crustal activities such as faulting and earthquakes. As the geothermal water is heated at depth, it dissolves these gases and then rises along the fault, accumulating at a depth of approximately 2 km before being extracted to the surface through geothermal wells.

The gas evolution in fault-controlled geothermal systems is a key factor in understanding the formation and distribution of valuable resources like H_2 and CH_4. In non-volcanic regions lacking ophiolites and peridotite massifs, geothermal fluids circulating through active fault-controlled systems typically contain H_2 and CH_4. Along the XSHF, one of the most active intracontinental faults globally, the highest volumetric concentrations of H_2 and CH_4 are 1.69 % and 3.97 %, respectively. However, these values are much lower than the concentration threshold (10 %) generally considered to have viable resource potential [15,142]. This relatively low content is attributed to both the formation mechanisms of the material sources and regional tectonic conditions. The amount of CH_4 is primarily influenced by the abundance of organic matter in sedimentary rocks and infiltrating groundwater, as well as the thermogenic conditions along the groundwater flow path. In contrast, H_2 production depends on factors such as lithology, rock fragmentation, fault activity, and hydrothermal conditions. Additionally, the absence of a stable reservoir with a cap rock (a geological seal barrier) in fault-controlled areas prevents H_2 and CH_4 from accumulating in significant quantities, as the gases tend to migrate and leak continuously along the fractures. Thus, while H_2 and CH_4 are present in geothermal fluids near active fault zones, their resource potential is lower compared to regions with exposed ophiolites and peridotite massifs. In these areas, serpentinization of mafic and ultramafic rocks—especially those that produce H_2—represents a key exploration target [143]. For instance, the intense degassing of H_2 (84 % by volume) from the deep underground Bulqize chromite mine in Albania is attributed to the presence of a faulted reservoir deeply rooted in the Jurassic ophiolite massif [144].

6. Conclusions

This study identified the sources of hydrogen (H_2) and methane (CH_4) along the strike-slip XSHF in the eastern Tibetan Plateau, based on the chemical and isotope compositions, as well as the kinetic and thermodynamic data of hydrothermal fluids.

Our findings show that: H_2 is primarily generated through the hydrolysis of silicates during the destruction and fragmentation of rock on the fault plane surfaces under high-temperature conditions. Consequently, H_2 concentrations increase towards the southeastern end of the fault, correlating positively with Rc/Ra ratios, reservoir temperatures, slip rates, locking depths, and earthquake frequency and intensity along the fault. Methane, with the exception of a sample from Luhuo, which is mainly microbial in origin, is predominantly derived from the

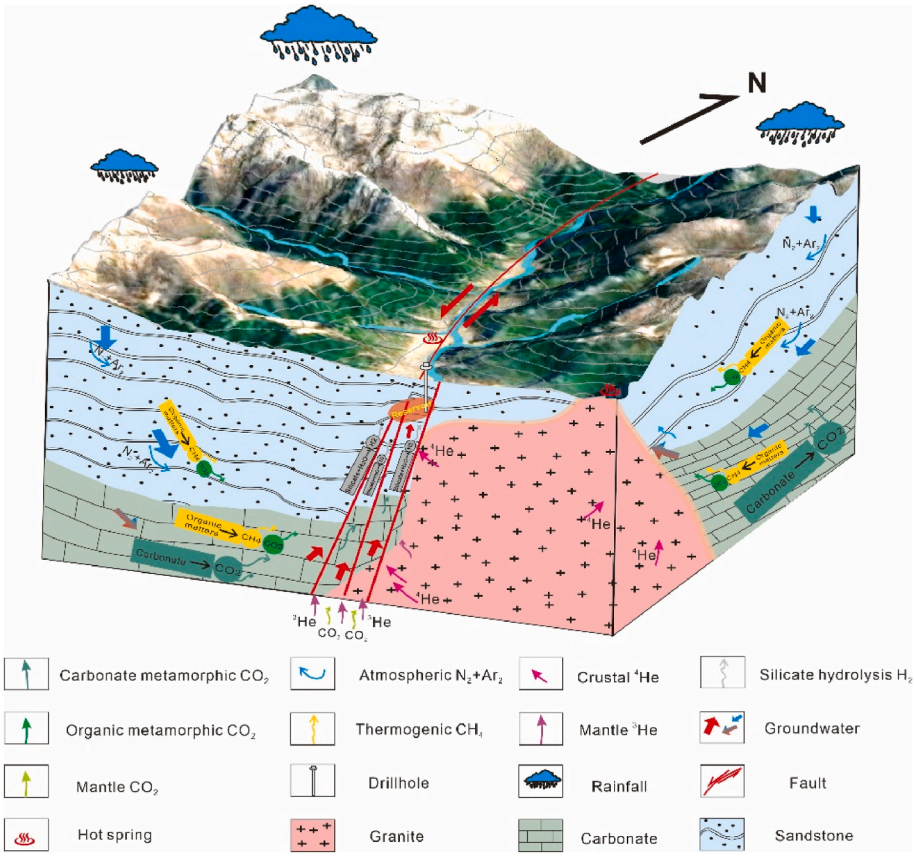

Fig. 10. Conceptual model for hydrothermal volatiles evolution in Yulingong geothermal system.

thermogenic transformation of organic matter buried in the sedimentary layers or carried by circulating groundwater. Evidence of organic matter metamorphism is indicated by a 10–20 % contribution of organic metamorphism to the total CO_2 carbon inventory. In the H_2-H_2O-CH_4-CO_2 system of geothermal fluids, rapid isotope exchange between CH_4-H_2 and H_2O-H_2 preserves information about the reservoir conditions in fluids that rise quickly to the surface. This confirms that the drillhole at Yulingong has penetrated the geothermal reservoir at a depth of 2006 m. However, isotope exchange between CH_4-H_2O and CO_2-CH_4 is typically far from equilibrium due to slower kinetics. Both H_2 and CH_4 are commonly present in fault-controlled hydrothermal systems. H_2 is predominantly generated through water-rock interactions at fault zone surfaces, where fresh rock is exposed by fault activity. CH_4 production depends on trace amounts of organic matter in surrounding rock or groundwater. These formation processes take place within the fracture system of the fault zone, which lacks the cap rock and reservoir space typical of sedimentary basins. As a result, substantial gas reservoirs are unlikely to develop, limiting the potential for large-scale extraction and utilization.

These findings enhance the understanding of hydrogen and methane genesis and their resource potential, especially in non-volcanic geothermal areas controlled by active faults, both within the Tibetan Plateau and globally, where ophiolites and peridotite massifs are absent. The insights provide valuable implications for exploring clean, renewable energy resources in similar continental orogenic regions worldwide.

CRediT authorship contribution statement

Jiao Tian: Writing – original draft, Visualization, Software, Methodology, Conceptualization. **Yinlei Hao:** Writing – review & editing, Methodology, Investigation. **Yingchun Wang:** Writing – review & editing, Investigation. **Dawei Liao:** Writing – review & editing, Investigation. **Lantian Xing:** Writing – review & editing, Data curation. **Chunhui Cao:** Writing – review & editing, Data curation. **Ying Li:** Writing – review & editing, Methodology. **Xiaocheng Zhou:** Writing – review & editing, Project administration, Funding acquisition, Data curation. **Zhonghe Pang:** Writing – review & editing, Project administration, Funding acquisition.

Declaration of competing interest

To the best of our knowledge, the named authors have no known competing financial interests or personal relationships that could have appeared to influence the work reported in this paper.

Acknowledgements

We would like to express our sincere gratitude to Professor Zhang Jian from University of the Chinese Academy of Sciences for his encouragement and guidance throughout the writing process. The work was funded by the National Natural Science Foundation of China (42130809, 41902252), the Deep-land National Science and Technology Major Project (2024ZD1000503), Institution Basal Research Fund of the Institute of Earthquake Forecasting, China Earthquake Administration (CEAIEF20240210), IGCP Project 724.

Appendix A. Supplementary data

Supplementary data to this article can be found online at https://doi.org/10.1016/j.renene.2025.123991.

References

[1] A.S. Bradley, The sluggish speed of making abiotic methane, P. Natl. Acad Sci. USA. 113 (49) (2016) 13944–13946, https://doi.org/10.1073/pnas.1617103113.
[2] J. Telling, E. Boyd, N. Bone, E. Jones, M. Tranter, J. MacFarlane, P.G. Martin, J. Wadham, G. Lamarche-Gagnon, M. Skidmore, Rock comminution as a source of hydrogen for subglacial ecosystems, Nat. Geosci. 8 (11) (2015) 851–855, https://doi.org/10.1038/ngeo2533.
[3] L. Truche, T.M. McCollom, I. Martinez, Hydrogen and abiotic hydrocarbons: molecules that change the world, Elements 16 (1) (2020) 13–18, https://doi.org/10.2138/gselements.16.1.13.
[4] B. Ménez, Abiotic hydrogen and methane: fuels for life, Elements 16 (1) (2020) 39–46, https://doi.org/10.2138/gselements.16.1.39.
[5] E.P. Reeves, J. Fiebig, Abiotic synthesis of methane and organic compounds in Earth's lithosphere, Elements 16 (1) (2020) 25–31, https://doi.org/10.2138/gselements.16.1.25.
[6] S. Han, Z. Tang, C. Wang, B. Horsfield, T. Wang, N. Mahlstedt, Hydrogen-rich gas discovery in Continental scientific drilling project of songliao basin, northeast China: new insights into deep Earth exploration, Sci. Bull. 67 (10) (2022) 1003–1006, https://doi.org/10.1016/j.scib.2022.02.008.
[7] K. Kostúr, J. Kačur, Indirect measurement of syngas calorific value, in: Proceedings Proceedings of the 2015 16th International Carpathian Control Conference (ICCC), IEEE, 2015, pp. 229–234, https://doi.org/10.1109/CarpathianCC.2015.7145079.
[8] M. Muñoz-Guillena, A. Linares-Solano, C.S.M. De Lecea, Determination of calorific values of coals by differential thermal analysis, Fuel 71 (5) (1992) 579–583, https://doi.org/10.1016/0016-2361(92)90157-J.
[9] O. Nwufo, O. Nwafor, J. Igbokwe, Effects of blends on the physical properties of bioethanol produced from selected Nigerian crops, Int. J. Ambient Energy 37 (1) (2016) 10–15, https://doi.org/10.1080/01430750.2013.866907.
[10] F. Tassi, J. Fiebig, O. Vaselli, M. Nocentini, Origins of methane discharging from volcanic-hydrothermal, geothermal and cold emissions in Italy, Chem. Geol. 310 (2012) 36–48, https://doi.org/10.1016/j.chemgeo.2012.03.018.
[11] A. Vitale Brovarone, I. Martinez, A. Elmaleh, R. Compagnoni, C. Chaduteau, C. Ferraris, I. Esteve, Massive production of abiotic methane during subduction evidenced in metamorphosed ophicarbonates from the Italian alps, Nat. Commun. 8 (1) (2017) 14134, https://doi.org/10.1038/ncomms14134.
[12] G. Etiope, M. Schoell, Abiotic gas: atypical, but not rare, Elements 10 (4) (2014) 291–296, https://doi.org/10.2113/gselements.10.4.291.
[13] G. Etiope, Abiotic methane in Continental serpentinization sites: an overview, Proc. Earth Planet. Sci. 17 (2017) 9–12, https://doi.org/10.1016/j.proeps.2016.12.006.
[14] G. Etiope, B. Sherwood Lollar, Abiotic methane on Earth, Rev. Geophys. 51 (2) (2013) 276–299, https://doi.org/10.1002/rog.20011.
[15] A.V. Milkov, Molecular hydrogen in surface and subsurface natural gases: Abundance, origins and ideas for deliberate exploration, Earth Sci. Rev. (2022) 104063, https://doi.org/10.1016/j.earscirev.2022.104063.
[16] T. Abrajano, N. Sturchio, J. Bohlke, G. Lyon, R. Poreda, C. Stevens, Methane-hydrogen gas seeps, Zambales ophiolite, Philippines: deep or shallow origin? Chem. Geol. 71 (1–3) (1988) 211–222, https://doi.org/10.1016/0009-2541(88)90116-7.
[17] G. Etiope, M. Schoell, H. Hosgörmez, Abiotic methane flux from the chimaera seep and tekirova ophiolites (turkey): understanding gas exhalation from low temperature serpentinization and implications for Mars, Earth Planet Sci. Lett. 310 (1) (2011) 96–104, https://doi.org/10.1016/j.epsl.2011.08.001.
[18] T.O. Stevens, J.P. Mckinley, Abiotic controls on H_2 production from basalt−water reactions and implications for aquifer biogeochemistry, Environ. Sci. Technol. 35 (7) (2000) 826–831, https://doi.org/10.1021/es990583g.
[19] T. Boschetti, G. Etiope, L. Toscani, Abiotic methane in the hyperalkaline springs of Genova, Italy, Proc. Earth Planet. Sci. 7 (2013) 248–251, https://doi.org/10.1016/j.proeps.2013.02.004.
[20] A.S. Bradley, R.E. Summons, Multiple origins of methane at the lost city hydrothermal field, Earth Planet Sci. Lett. 297 (1) (2010) 34–41, https://doi.org/10.1016/j.epsl.2010.05.034.
[21] J.L. Charlou, J.P. Donval, Y. Fouquet, P. Jean-Baptiste, N. Holm, Geochemistry of high H_2 and CH_4 vent fluids issuing from ultramafic rocks at the rainbow hydrothermal field (36°14′N, MAR), Chem. Geol. 191 (4) (2002) 345–359, https://doi.org/10.1016/S0009-2541(02)00134-1.
[22] J.L. Charlou, J.P. Donval, C. Konn, H. Ondréas, Y. Fouquet, P. Jean-Baptiste, E. Fourré, High production and fluxes of H_2 and CH_4 and evidence of abiotic hydrocarbon synthesis by serpentinization in ultramafic-hosted hydrothermal systems on the mid-atlantic ridge, Geophys. Monogr. 188 (2010) 265–296, https://doi.org/10.1029/2008GM000752.
[23] Y. Hao, Z. Pang, J. Tian, Y. Wang, Z. Li, L. Li, L. Xing, Origin and evolution of hydrogen-rich gas discharges from a hot spring in the eastern coastal area of China, Chem. Geol. 538 (2020) 119477, https://doi.org/10.1016/j.chemgeo.2020.119477.
[24] V. Zgonnik, The occurrence and geoscience of natural hydrogen: a comprehensive review, Earth Sci. Rev. 203 (2020) 103140, https://doi.org/10.1016/j.earscirev.2020.103140.
[25] S.L. Klemperer, P. Zhao, C.J. Whyte, T.H. Darrah, L.J. Crossey, K.E. Karlstrom, T. Liu, C. Winn, D.R. Hilton, L. Ding, Limited underthrusting of India below Tibet: $^3He/^4He$ analysis of thermal springs locates the mantle suture in continentaC collision, P. Natl. Acad Sci. USA. 119 (12) (2022) e2113877119, https://doi.org/10.1073/pnas.2113877119.

[26] Z. Liao, P. Zhao, Yunnan-tibet geothermal belt-geothermal resources and case histories, Science (1999). Beijing (in Chinese with English abstract).
[27] S. Wang, X. Zhou, J. Tian, M. He, J. Li, J. Dong, L. Li, Z. Li, L. Xing, G. Zheng, Constraints on geological structures and dynamics along the tian Shan-Pamir orogenic belt with helium isotopes in hot springs, Appl. Geochem. 160 (2024) 105859, https://doi.org/10.1016/j.apgeochem.2023.105859.
[28] Y. Bai, Z. Shi, X. Zhou, C. Wu, G. Wang, M. He, J. Li, J. Dong, J. Tian, Y. Yan, Gas geochemical evidence for the India-Asia lithospheric transition boundary near the karakorum fault in western Tibet, Chem. Geol. 639 (2023) 121728, https://doi.org/10.1016/j.chemgeo.2023.121728.
[29] Y. Li, X. Zhou, T. Huang, J. Tian, M. He, X. Zhu, J. Li, Y. Zhang, Z. Wu, B. Li, Origins of volatiles and helium fluxes from hydrothermal systems in the eastern himalayan syntaxis and constraints on regional heat and tectonic activities, J. Hydrol. (2024) 130776, https://doi.org/10.1016/j.jhydrol.2024.130776.
[30] D.L. Newell, M.J. Jessup, J.M. Cottle, D.R. Hilton, Z.D. Sharp, T.P. Fischer, Aqueous and isotope geochemistry of mineral springs along the southern margin of the Tibetan plateau: implications for fluid sources and regional degassing of CO_2, G-cubed 9 (8) (2008) 1–20, https://doi.org/10.1029/2008GC002021.
[31] M. Zhang, Z. Guo, L. Zhang, Y. Sun, Z. Cheng, Geochemical constraints on origin of hydrothermal volatiles from southern Tibet and the himalayas: understanding the degassing systems in the India-Asia continental subduction zone, Chem. Geol. 469 (2017) 19–33, https://doi.org/10.1016/j.chemgeo.2017.02.023.
[32] W. Zhao, Z. Guo, G. Zheng, D.L. Pinti, M. Zhang, J. Li, L. Ma, Subducting Indian lithosphere controls the deep carbon emission in lhasa terrane, southern Tibet, J. Geophys. Res. Solid Earth 127 (2022) e2022JB024250, https://doi.org/10.1029/2022JB024250.
[33] P. Zhao, E. Xie, J. Duo, J. Jin, X. Hu, S. Du, Z. Yao, Geochemical characteristics of geothermal gases and their geological implications in Tibet, act, Petrol. Sin. 18 (4) (2002) 539–550 (in Chinese with English abstract).
[34] Y. Wang, X. Zhou, J. Tian, J. Zhou, M. He, J. Li, J. Dong, Y. Yan, F. Liu, B. Yao, Volatile characteristics and fluxes of He-CO_2 systematics in the southeastern Tibetan Plateau: constraints on regional seismic activities, J. Hydrol. 617 (2023) 129042, https://doi.org/10.1016/j.jhydrol.2022.129042.
[35] M. Zhang, S. Xu, X. Zhou, A. Caracausi, Y. Sano, Z. Guo, G. Zheng, Y.C. Lang, C. Q. Liu, Deciphering a mantle degassing transect related with India-Asia continental convergence from the perspective of volatile origin and outgassing, Geochem. Cosmochim. Acta 310 (2021) 61–78, https://doi.org/10.1016/j.gca.2021.07.010.
[36] Y. Fan, Z. Pang, D. Liao, J. Tian, Y. Hao, T. Huang, Y. Li, Hydrogeochemical characteristics and genesis of geothermal water from the ganzi geothermal field, eastern Tibetan Plateau, Water 11 (8) (2019) 1631, https://doi.org/10.3390/w11081631.
[37] J. Tian, Z. Pang, Q. Guo, Y. Wang, J. Li, T. Huang, Y. Kong, Geochemistry of geothermal fluids with implications on the sources of water and heat recharge to the rekeng high-temperature geothermal system in the eastern himalayan syntax, Geothermics 74 (2018) 92–105, https://doi.org/10.1016/j.geothermics.2018.02.006.
[38] J. Tian, Z. Pang, Y. Wang, Q. Guo, Fluid geochemistry of the cuopu high temperature geothermal system in the eastern himalayan syntaxis with implication on its genesis, Appl. Geochem. 110 (2019) 104422, https://doi.org/10.1016/j.apgeochem.2019.104422.
[39] J. Tian, Z. Pang, D. Liao, X. Zhou, Fluid geochemistry and its implications on the role of deep faults in the genesis of high temperature systems in the eastern edge of the Qinghai Tibet Plateau, Appl. Geochem. 131 (2021) 105036, https://doi.org/10.1016/j.apgeochem.2021.105036.
[40] X. Zhou, L. Liu, Z. Chen, Y. Cui, J. Du, Gas geochemistry of the hot spring in the litang fault zone, southeast Tibetan Plateau, Appl. Geochem. 79 (2017) 17–26, https://doi.org/10.1016/j.apgeochem.2017.01.022.
[41] F. Liu, J. Yang, D. Lian, G. Li, Geological features of neothyan ophiolites in Tibetan Plateau and its tectonic evolution, act, Petrol. Sin. 36 (10) (2020) 2913–2945 (in Chinese with English abstract).
[42] X. Sun, P. Jian, The wilson cycle of the jinshajiang paleo-tethys ocean, in Western Yunnan and Western Sichuan Province, Geol. Rev. 50 (4) (2004) 343–350 (in Chinses with English abstract).
[43] Y. Li, C. Wang, J. Dai, G. Xu, Y. Hou, X. Li, Propagation of the deformation and growth of the tibetan–himalayan orogen: a review, Earth Sci. Rev. 143 (2015) 36–61, https://doi.org/10.1016/j.earscirev.2015.01.001.
[44] S. Akciz, B.C. Burchfiel, J.L. Crowley, J. Yin, L. Chen, Geometry, kinematics, and regional significance of the chong Shan shear zone, eastern himalayan syntaxis, Yunnan, China, Geosphere 4 (1) (2008) 292–314, https://doi.org/10.1130/GES00111.1.
[45] C.Y. Wang, H. Lou, P.G. Silver, L. Zhu, L. Chang, Crustal structure variation along 30 N in the eastern Tibetan Plateau and its tectonic implications, Earth Planet Sci. Lett. 289 (3) (2010) 367–376, https://doi.org/10.1016/j.epsl.2009.11.026.
[46] P. Zhang, Q. Deng, G. Zhang, J. Ma, W. Gan, W. Min, F. Mao, Q. Wang, Active tectonic blocks and strong earthquakes in the continent of China, Sci. China SerD-Earth Sci. 46 (2) (2003) 13–24, https://doi.org/10.1360/03dz0002.
[47] C.R. Allen, L. Zhuoli, Q. Hong, X. Wen, H. Zhou, W. Huang, Field study of a highly active fault zone: the xianshuihe fault of Southwestern China, Geol. Soc. Am. Bull. 103 (9) (1991) 1178–1199, https://doi.org/10.1130/0016-7606(1991)103<1178:FSOAHA>2.3.CO;2.
[48] Q. Deng, P. Zhang, Y. Ran, X. Yang, W. Min, L. Chen, Active tectonics and earthquake activities in China, Earth Sci. Front. 10 (2003) 67–73 (in Chinese with English abstract).
[49] M. Bai, M.L. Chevalier, P.H. Leloup, H. Li, J. Pan, A. Replumaz, S. Wang, K. Li, Q. Wu, F. Liu, J. Zhang, Spatial slip rate distribution along the SE xianshuihe fault, eastern Tibet, and earthquake hazard assessment, Tectonics 40 (11) (2021) e2021TC006985, https://doi.org/10.1029/2021TC006985.
[50] L. Chen, H. Wang, Y. Ran, X. Sun, G. Su, J. Wang, X. Tan, Z. Li, X. Zhang, The MS 7.1 yushu earthquake surface rupture and large historical earthquakes on the garzê-yushu fault, Chin. Sci. Bull. 55 (31) (2010) 3504–3509, https://doi.org/10.1007/s11434-010-4079-2.
[51] R. Zhou, Y. He, Z. Huang, X. Li, T. Yang, The slip rate and strong earthquake recurrence interval on the qianning-kangding segment of the xianshuihe fault zone, Acta Seismol. Sin. 14 (3) (2001) 263–273, https://doi.org/10.1007/s11589-001-0004-8.
[52] Y.Z. Zhang, A. Replumaz, G.C. Wang, P.H. Leloup, C. Gautheron, M. Bernet, P.V. D. Beek, J.L. Paquette, A. Wang, K.X. Zhang, Timing and rate of exhumation along the litang fault system, implication for fault reorganization in southeast Tibet, Tectonics 34 (6) (2015) 1219–1243, https://doi.org/10.1002/2014TC003671.
[53] C. Wang, W.W. Chan, R. Mooney, Three-dimensional velocity structure of crust and upper mantle in southwestern China and its tectonic implications, J. Geophys. Res. Solid Earth 108 (9) (2003) 2442, https://doi.org/10.1029/2002JB001973.
[54] C. Wang, W. Han, J. Wu, H. Lou, W. Chan, Crustal structure beneath the eastern margin of the Tibetan Plateau and its tectonic implications, J. Geophys. Res. Solid Earth 112 (B7) (2007) 1–21, https://doi.org/10.1029/2005JB003873.
[55] C. Wang, L. Zhu, H. Lou, B. Huang, Z. Yao, X. Luo, Crustal thicknesses and Poisson's ratios in the eastern Tibetan Plateau and their tectonic implications, J. Geophys. Res. Solid Earth 115 (2010) B11301, https://doi.org/10.1029/2010JB007527.
[56] C.J. Wilson, M.J. Harrowfield, A.J. Reid, Brittle modification of Triassic architecture in eastern Tibet: implications for the construction of the Cenozoic plateau, J. Asian Earth Sci. 27 (3) (2006) 341–357, https://doi.org/10.1016/j.jseaes.2005.04.004.
[57] Z. Xu, L. Hou, Z. Wang, New progress in structural research of songpan-ganzi orogenic belt, China Geol 12 (1991) 14–16 (in Chinese with English abstract).
[58] F. Roger, M. Jolivet, J. Malavieille, The tectonic evolution of the songpan-garzê (north Tibet) and adjacent areas from Proterozoic to present: a synthesis, J. Asian Earth Sci. 39 (4) (2010) 254–269, https://doi.org/10.1016/j.jseaes.2010.03.008.
[59] Z. Hou, L. Wang, Z. Khin, X. Mo, M. Wang, D. Li, G. Pan, Post-collisional crustal extension setting and VHMS mineralization in the jinshajiang orogenic belt, southwestern China, Ore Geol. Rev. 22 (3–4) (2003) 177–199, https://doi.org/10.1016/S0169-1368(02)00141-5.
[60] H. Li, Y. Zhang, Zircon U–Pb geochronology of the konggar granitoid and migmatite: constraints on the Oligo-Miocene tectono-thermal evolution of the xianshuihe fault zone, east Tibet, Tectonophysics 606 (2013) 127–139, https://doi.org/10.1016/j.tecto.2013.07.007.
[61] G. Jiang, S. Hu, Y. Shi, C. Zhang, Z. Wang, D. Hu, Terrestrial heat flow of continental China: updated dataset and tectonic implications, Tectonophysics 753 (2019) 36–48, https://doi.org/10.1016/j.tecto.2019.01.006.
[62] M. Xu, C. Zhu, S. Rao, S. Hu, Difference of thermal structure between eastern edge of Tibet Plateau and western sichuan basin, Chinese J. Geol. 46 (1) (2012) 203–212 (in Chinese with English abstract).
[63] Q. Guo, Z. Pang, Y. Wang, J. Tian, Fluid geochemistry and geothermometry applications of the kangding high-temperature geothermal system in eastern himalayas, Appl. Geochem. 81 (2017) 63–75, https://doi.org/10.1016/j.apgeochem.2017.03.007.
[64] S. Arnórsson, J.Ö. Bjarnason, N. Giroud, I. Gunnarsson, A. Stefánsson, Sampling and analysis of geothermal fluids, Geofluids 6 (3) (2006) 203–216, https://doi.org/10.1111/j.1468-8123.2006.00147.x.
[65] Y. Sano, B. Marty, Origin of carbon from fumarolic gas in island arc, Chem. Geol. 119 (1) (1995) 265–274, https://doi.org/10.1016/0009-2541(94)00097-R.
[66] W. Giggenbach, A simple method for the collection and analysis of volcanic gas samples, Bull. Volcanol. 39 (1) (1975) 132–145, https://doi.org/10.1007/BF02596953.
[67] M. Zhang, Z. Guo, Y. Sano, L. Zhang, Y. Sun, Z. Cheng, T.F. Yang, Magma-derived CO_2 emissions in the tengchong volcanic field, SE Tibet: implications for deep carbon cycle at intra-continent subduction zone, J. Asian Earth Sci. 127 (2016) 76–90, https://doi.org/10.1016/j.jseaes.2016.06.009.
[68] D. Tardani, M. Reich, E. Roulleau, N. Takahata, Y. Sano, P. Pérez-Flores, P. Sánchez-Alfaro, J. Cembrano, G. Arancibia, Exploring the structural controls on helium, nitrogen and carbon isotope signatures in hydrothermal fluids along an intra-arc fault system, Geochem. Cosmochim. Acta 184 (2016) 193–211, https://doi.org/10.1016/j.gca.2016.04.031.
[69] Y. Sano, H. Wakita, Geographical distribution of $^3He/^4He$ ratios in Japan: implications for arc tectonics and incipient magmatism, J. Geophys. Res. Solid Earth 90 (B10) (1985) 8729–8741, https://doi.org/10.1029/JB090iB10p08729.
[70] Y. Kong, K. Wang, J. Li, Z. Pang, Stable isotopes of precipitation in China: a consideration of moisture sources, Water 11 (6) (2019) 1239, https://doi.org/10.3390/w11061239.
[71] J.E. Lupton, Terrestrial inert gases-isotope tracer studies and clues to primordial components in the mantle, Annu. Rev. Earth Planet Sci. 11 (1983) 371–414.
[72] D.W. Graham, Noble gas isotope geochemistry of mid-ocean ridge and ocean island basalts: characterization of mantle source reservoirs, Rev. Mineral. Geochem. 47 (1) (2002) 247–317, https://doi.org/10.2138/rmg.2002.47.8.
[73] J.M. Day, P.H. Barry, D.R. Hilton, R. Burgess, D.G. Pearson, L.A. Taylor, The helium flux from the continents and ubiquity of low-$^3He/^4He$ recycled crust and lithosphere, Geochem. Cosmochim. Acta 153 (2015) 116–133, https://doi.org/10.1016/j.gca.2015.01.008.

[74] H. Karakuş, Helium and carbon isotope composition of gas discharges in the simav geothermal field, Turkey: implications for the heat source, Geothermics 57 (2015) 213–223, https://doi.org/10.1016/j.geothermics.2015.07.005.
[75] P. Zhao, J. Dor, T. Liang, J. Jin, H. Zhang, Characteristics of gas geochemistry in yangbajing geothermal field, Tibet, Chin. Sci. Bull. 43 (21) (1998) 1770–1777, https://doi.org/10.1007/BF02883369.
[76] R. O'nions, E. Oxburgh, Helium, volatile fluxes and the development of continental crust, Earth Planet Sci. Lett. 90 (3) (1988) 331–347, https://doi.org/10.1016/0012-821X(88)90134-3.
[77] S.M. Gilfillan, C.J. Ballentine, G. Holland, D. Blagburn, B.S. Lollar, S. Stevens, M. Schoell, M. Cassidy, The noble gas geochemistry of natural CO_2 gas reservoirs from the colorado Plateau and rocky Mountain provinces, USA, Geochem. Cosmochim. Acta 72 (4) (2008) 1174–1198, https://doi.org/10.1016/j.gca.2007.10.009.
[78] M. Zhang, L. Zhang, W. Zhao, Z. Guo, S. Xu, Y. Sano, Y.C. Lang, C.Q. Liu, Y. Li, Metamorphic CO_2 emissions from the southern yadong-gulu rift, Tibetan Plateau: insights into deep carbon cycle in the India-Asia Continental collision zone, Chem. Geol. 584 (2021) 120534, https://doi.org/10.1016/j.chemgeo.2021.120534.
[79] S. Arnorsson, Mineral deposition from Icelandic geothermal waters: environmental and utilization problems, J. Petrol. Technol. 33 (1) (1981) 181–187, https://doi.org/10.2118/7890-PA.
[80] P.H. Barry, R. Negrete-Aranda, R.M. Spelz, A.M. Seltzer, D.V. Bekaert, C. Virrueta, J.T. Kulongoski, Volatile sources, sinks and pathways: a helium-carbon isotope study of Baja California fluids and gases, Chem. Geol. 550 (2020) 119722, https://doi.org/10.1016/j.chemgeo.2020.119722.
[81] J.R. Holloway, J.G. Blank, Application of experimental results to COH species in natural melts, Rev. Mineral. 30 (1994) 187, https://doi.org/10.1515/9781501509674-012, 187.
[82] H. Ohmoto, R.O. Rye, H.L. Barnes (Eds.), Geochemistry of Hydrothermal Ore Deposits, 1979, pp. 509–567.
[83] Z. Guo, M. Wilson, Late Oligocene–early Miocene transformation of postcollisional magmatism in Tibet, Geology 47 (8) (2019) 776–780, https://doi.org/10.1130/G46147.1.
[84] S. Xu, L. Guan, M. Zhang, J. Zhong, W. Liu, X.G. Xie, C. Liu, N. Takahata, Y. Sano, Degassing of deep-sourced CO_2 from xianshuihe-anninghe fault zones in the eastern Tibetan Plateau, Sci. China Earth Sci. 65 (1) (2022) 139–155, https://doi.org/10.1007/s11430-021-9810-x.
[85] T. Plank, C.E. Manning, Subducting carbon, Nature 574 (2019) 343–352, https://doi.org/10.1038/s41586-019-1643-z.
[86] S. Shen, C. Cao, Y. Zhang, W. Li, G.R. Shi, Y. Wang, Y. Wu, K. Ueno, C. M. Henderson, X. Wang, End-permian mass extinction and palaeoenvironmental changes in neotethys: evidence from an oceanic carbonate section in southwestern Tibet, Global Planet. Change 73 (1) (2010) 3–14, https://doi.org/10.1016/j.gloplacha.2010.03.007.
[87] N.J.P. Smith, T.J. Shepherd, M.T. Styles, G.M. Williams, Hydrogen exploration: a review of global hydrogen accumulations and implications for prospective areas in NW Europe, in: Pet. Geol. North-West Eur. Glob. Perspect. - Proc. 6th Pet. Geol. Conf., 6, Geological Society, London, 2005, pp. 349–358, https://doi.org/10.1144/0060349.
[88] N. Akhlaghi, G. Najafpour-Darzi, A comprehensive review on biological hydrogen production, Int. J. Hydrogen Energy 45 (43) (2020) 22492–22512, https://doi.org/10.1016/j.ijhydene.2020.06.182.
[89] K. Kashefi, D.R. Lovley, Extending the upper temperature limit for life, Science 301 (5635) (2003) 934, https://doi.org/10.1126/science.1086823, 934.
[90] W. Tong, Z. Mu, S. Liu, The late-cenozoic volcanoes and active high-temperature hydrothermal systems in China, act, Geophys. Sin. 33 (3) (1990) 329–335 (in Chinese with English abstract).
[91] A.L. Day, E.S. Shepherd, Water and volcanic activity, Geol. Soc. Am. Bull. 24 (1913) 573–606, https://doi.org/10.1130/GSAB-24-573.
[92] J. Tian, X. Zhou, M. Liao, M. He, Z. Zeng, Y. Yan, B. Yao, Y. Wang, S. Cui, G. Xing, C. Cao, L. Li, C. Ju, Tectonic variations in NS-trending rifts, southern Tibetan Plateau: insights from hydrothermal emissions and seismic activities, J. Asian Earth Sci. 287 (2025) 106599, https://doi.org/10.1016/j.jseaes.2025.106599.
[93] C. Wu, S. Ji, H. Cao, H. Dong, X. Chen, Jurassic post-collisional extension in the songpan–ganze terrane, eastern Tibetan Plateau: evidence from weakly peraluminous a-type granites within the zheduo–gongga massif, Geol. J. 56 (2021) 1911–1931, https://doi.org/10.1002/gj.4034.
[94] K.H. Wedepohl, The composition of the continental crust, Geochem. Cosmochim. Acta 59 (1995) 1217–1232, https://doi.org/10.1016/0016-7037(95)00038-2.
[95] L.H. Lin, G.F. Slater, B.S. Lollar, C.G. Lacrampe, T.C. Onstott, The yield and isotopic composition of radiolytic H_2, a potential energy source for the deep subsurface biosphere, Geochem. Cosmochim. Acta 69 (2005) 893–903, https://doi.org/10.1016/j.gca.2004.07.032.
[96] I. Kita, S. Matsuo, H. Wakita, H_2 generation by reaction between H_2O and crushed rock: an experimental study on H_2 degassing from the active fault zone, J. Geophys. Res. Solid Earth 87 (B13) (1982) 10789–10795, https://doi.org/10.1029/JB087iB13p10789.
[97] F.T. Freund, M.M. Freund, Paradox of peroxy defects and positive holes in rocks. Part I: effect of temperature, J. Asian Earth Sci. 114 (2015) 373–383, https://doi.org/10.1016/j.jseaes.2015.04.047.
[98] T. Dogan, T. Mori, F. Tsunomori, K.J.P. Notsu, A. Geophysics, Soil H_2 and CO_2 surveys at several active faults in Japan, Pure Appl. Geophys. 164 (12) (2007) 2449–2463, https://doi.org/10.1007/978-3-7643-8720-4_6.
[99] T. Hirose, S. Kawagucci, K. Suzuki, Mechanoradical H_2 generation during simulated faulting: implications for an earthquake-driven subsurface biosphere, Geophys. Res. Lett. 38 (17) (2011) 245–255, https://doi.org/10.1029/2011GL048850.
[100] M. Sato, A. Sutton, K. McGee, Anomalous hydrogen emissions from the san andreas fault observed at the cienega winery, central California, Pure Appl. Geophys. 122 (1984) 376–391, https://doi.org/10.1007/BF00874606.
[101] H. Wakita, Y. Nakamura, I. Kita, N. Fujii, K. Notsu, Hydrogen release: new indicator of fault activity, Science 210 (4466) (1980) 188–190, https://doi.org/10.1126/science.210.4466.188.
[102] X. Zhou, J. Du, Z. Chen, J. Cheng, Y. Li, Geochemistry of soil gas in the seismic fault zone produced by the wenchuan Ms 8.0 earthquake, southwestern China, Geochem. Trans. 11 (2010) 5, https://doi.org/10.1186/1467-4866-11-5.
[103] J. Kameda, K. Saruwatari, H. Tanaka, F.J.E. Tsunomori, Planets, space, mechanisms of hydrogen generation during the mechanochemical treatment of biotite within D_2O media, Earth Planets Space 56 (12) (2004) 1241–1245, https://doi.org/10.1186/BF03353346.
[104] R.J. Parkes, S. Berlendis, E.G. Roussel, H. Bahruji, G. Webster, A. Oldroyd, A. J. Weightman, M. Bowker, P.R. Davies, H. Sass, Rock-crushing derived hydrogen directly supports a methanogenic community: significance for the deep biosphere, Environ. Microbiol. Rep. 11 (2019) 165–172, https://doi.org/10.1111/1758-2229.12723.
[105] X. Qiao, Y. Zhou, P. Zhang, Along-strike variation in fault structural maturity and seismic moment deficits on the yushu-ganzi-xianshuihe fault system revealed by strain accumulation and regional seismicity, Earth Planet Sci. Lett. 596 (2022) 117799, https://doi.org/10.1016/j.epsl.2022.117799.
[106] X. Qiao, Y. Zhou, Geodetic imaging of shallow creep along the xianshuihe fault and its frictional properties, Earth Planet Sci. Lett. 567 (2021) 117001, https://doi.org/10.1016/j.epsl.2021.117001.
[107] L. Han, Y. Zhou, C. He, H. Li, Sublithostatic pore fluid pressure in the brittle–ductile transition zone of Mesozoic yingxiu-beichuan fault and its implication for the 2008 Mw 7.9 wenchuan earthquake, J. Asian Earth Sci. 117 (2016) 107–118, https://doi.org/10.1016/j.jseaes.2015.12.009.
[108] M. Wang, Z. Shen, Present-day crustal deformation of continental China derived from GPS and its tectonic implications, J. Geophys. Res. Solid Earth 125 (2) (2020) e2019JB018774, https://doi.org/10.1029/2019JB018774.
[109] I. Kita, D/H ratios of H_2 in soil gases as an indicator of fault movements, Geochem. J. 14 (6) (1980) 317–320, https://doi.org/10.2343/geochemj.14.317.
[110] B. Bernard, J.M. Brooks, W.M. Sackett, A geochemical model for characterization of hydrocarbon gas sources in marine sediments, in: 9th Annual Offshore Technology Conference, 1977, pp. 435–438, https://doi.org/10.4043/2934-MS. OTC 2934.
[111] M. Schoell, Genetic characterization of natural gases, Am. Assoc. Petrol. Geol. Bull. 67 (1983) 2225–2238.
[112] M.J. Whiticar, E. Faber, M. Schoell, Biogenic methane formation in marine and freshwater environments: CO_2 reduction vs. acetate fermentation—Isotope evidence, Geochem. Cosmochim. Acta 50 (5) (1986) 693–709, https://doi.org/10.1016/0016-7037(86)90346-7.
[113] J. Fiebig, A. Stefansson, A. Ricci, F. Tassi, F. Viveiros, S. Silva, T. Lopez, C. Schreiber, S. Hofmann, B.W. Mountain, Abiogenesis not required to explain the origin of volcanic-hydrothermal hydrocarbons, Geochem. Persp. Let. 11 (2019) 23–27, https://doi.org/10.7185/geochemlet.1920.
[114] A.V. Milkov, G. Etiope, Revised genetic diagrams for natural gases based on a global dataset of> 20,000 samples, Org. Geochem. 125 (2018) 109–120, https://doi.org/10.1016/j.orggeochem.2018.09.002.
[115] A. Stefánsson, A. Ricci, M. Garnett, J. Gunnarsson-Robin, B.I. Kleine-Marshall, S. W. Scott, M. Lelli, C.D. Cardoso, R. Pik, C. Santinelli, S. Ono, P.H. Barry, M. W. Broadley, D. Byrne, S.A. Halldórsson, J. Fiebig, Isotopic and kinetic constraints on methane origins in Icelandic hydrothermal fluids, Geochem. Cosmochim. Acta 373 (2024) 84–97, https://doi.org/10.1016/j.gca.2024.03.015.
[116] G. Etiope, C. Oze, Microbial vs abiotic origin of methane in continental serpentinized ultramafic rocks: a critical review and the need of a holistic approach, Appl. Geochem. (2022) 105373, https://doi.org/10.1016/j.apgeochem.2022.105373.
[117] M.J. Whiticar, Carbon and hydrogen isotope systematics of bacterial formation and oxidation of methane, Chem. Geol. 161 (1–3) (1999) 291–314, https://doi.org/10.1016/S0009-2541(99)00092-3.
[118] K. Daskalopoulou, S. Calabrese, F. Grassa, K. Kyriakopoulos, F. Parello, F. Tassi, W. D'Alessandro, Origin of methane and light hydrocarbons in natural fluid emissions: a key study from Greece, Chem. Geol. 479 (2018) 286–301, https://doi.org/10.1016/j.chemgeo.2018.01.027.
[119] F. Fischer, H. Tropsch, Die Erdölsynthese bei gewöhnlichem Druck aus den Vergasungsprodukten der Kohlen. Brennst, Chem 7 (1926) 97–104.
[120] P. Sabatier, J. Senderens, Direct hydrogenation of oxides of carbon in presence of various finely divided metals, C. R. Acad. Sci. 134 (1) (1902) 689–691.
[121] J. Horita, M.E. Berndt, Abiogenic methane formation and isotopic fractionation under hydrothermal conditions, Science 285 (5430) (1999) 1055–1057, https://doi.org/10.1126/science.285.5430.1055.
[122] H. Ueda, Y. Matsui, Y. Sawaki, Abiotic methane generation via CO_2 hydrogenation with natural chromitite under hydrothermal conditions, G-cubed 22 (4) (2021) e2020GC009533, https://doi.org/10.1029/2020GC009533.
[123] C. Oze, L.C. Jones, J.I. Goldsmith, R.J. Rosenbauer, Differentiating biotic from abiotic methane genesis in hydrothermally active planetary surfaces, P. Natl. Acad Sci. USA. 109 (25) (2012) 9750–9754, https://doi.org/10.1073/pnas.1205223109.
[124] P.J. Lunde, F.L. Kester, Rates of methane formation from carbon dioxide and hydrogen over a ruthenium catalyst, J. Catal. 30 (3) (1973) 423–429, https://doi.org/10.1016/0021-9517(73)90159-0.

[125] K.R. Thampi, J. Kiwi, M. Gratzel, Methanation and photo-methanation of carbon dioxide at room temperature and atmospheric pressure, Nature 327 (6122) (1987) 506–508, https://doi.org/10.1038/327506a0.
[126] A.S. Bradley, J.M. Hayes, R.E. Summons, Extraordinary ^{13}C enrichment of diether lipids at the Lost City lydrothermal Field indicates a carbon-limited ecosystem, Geochem. Cosmochim. Acta 73 (1) (2009) 102–118, https://doi.org/10.1016/j.gca.2008.10.005.
[127] X. Xia, Y. Gao, Methane from microbial hydrogenolysis of sediment organic matter before the great oxidation event, Nat. Commun. 12 (1) (2021) 5032, https://doi.org/10.1038/s41467-021-25336-6.
[128] J.F. Barker, P. Fritz, Carbon isotope fractionation during microbial methane oxidation, Nature 293 (5830) (1981) 289–291, https://doi.org/10.1038/293289a0.
[129] K. Suda, Y. Ueno, M. Yoshizaki, H. Nakamura, K. Kurokawa, E. Nishiyama, K. Yoshino, Y. Hongoh, K. Kawachi, S. Omori, Origin of methane in serpentinite-hosted hydrothermal systems: the CH_4–H_2–H_2O hydrogen isotope systematics of the hakuba happo hot spring, Earth Planet Sci. Lett. 386 (2014) 112–125, https://doi.org/10.1016/j.epsl.2013.11.001.
[130] D.A. Stolper, M. Lawson, C.L. Davis, A.A. Ferreira, E.V.S. Neto, G.S. Ellis, M. D. Lewan, A.M. Martini, Y. Tang, M.J.S. Schoell, Formation temperatures of thermogenic and biogenic methane, Science 344 (6191) (2014) 1500–1503, https://doi.org/10.1126/science.1254509.
[131] B.B. Bernard, J.M. Brooks, W.M. Sackett, Light hydrocarbons in recent Texas continental shelf and slope sediments, J. Geophys. Res.: Oceans 83 (1978) 4053–4061, https://doi.org/10.1029/JC083iC08p04053.
[132] G. Proskurowski, M.D. Lilley, D.S. Kelley, E.J. Olson, Low temperature volatile production at the lost city hydrothermal field, evidence from a hydrogen stable isotope geothermometer, Chem. Geol. 229 (4) (2006) 331–343, https://doi.org/10.1016/j.chemgeo.2005.11.005.
[133] N.J. Pester, M.E. Conrad, K.G. Knauss, D.J. DePaolo, Kinetics of D/H isotope fractionation between molecular hydrogen and water, Geochem. Cosmochim. Acta 242 (2018) 191–212, https://doi.org/10.1016/j.gca.2018.09.015.
[134] Y. Horibe, H. Craig, DH fractionation in the system methane-hydrogen-water, Geochem. Cosmochim. Acta 59 (24) (1995) 5209–5217, https://doi.org/10.1016/0016-7037(95)00391-6.
[135] W.F. Giggenbach, Relative importance of thermodynamic and kinetic processes in governing the chemical and isotopic composition of carbon gases in high-heatflow sedimentary basins, Geochem. Cosmochim. Acta 61 (17) (1997) 3763–3785, https://doi.org/10.1016/S0016-7037(97)00171-3.
[136] J. Li, G. Yang, G. Sagoe, Y. Li, Major hydrogeochemical processes controlling the composition of geothermal waters in the kangding geothermal field, western Sichuan Province, Geothermics 75 (2018) 154–163, https://doi.org/10.1016/j.geothermics.2018.04.008.
[137] A. Ricci, B.I. Kleine, J. Fiebig, J. Gunnarsson-Robin, K.M. Kamunya, B. Mountain, A. Stefánsson, Equilibrium and kinetic controls on molecular hydrogen abundance and hydrogen isotope fractionation in hydrothermal fluids, Earth Planet Sci. Lett. 579 (2022) 117338, https://doi.org/10.1016/j.epsl.2021.117338.
[138] W.F. Giggenbach, Geothermal solute equilibria. derivation of Na-K-Mg-Ca geoindicators, Geochem. Cosmochim. Acta 52 (12) (1988) 2749–2765, https://doi.org/10.1016/0016-7037(88)90143-3.
[139] Y. Cheng, Z. Pang, Y. Kong, X. Chen, G. Wang, Imaging the heat source of the kangding high-temperature geothermal system on the xianshuihe fault by magnetotelluric survey, Geothermics 102 (2022) 102386, https://doi.org/10.1016/j.geothermics.2022.102386.
[140] A.C. Turner, N.J. Pester, M. Bill, M.E. Conrad, K.G. Knauss, D. Astolper, Experimental determination of hydrogen isotope exchange rates between methane and water under hydrothermal conditions, Geochem. Cosmochim. Acta 329 (2022) 231–255, https://doi.org/10.1016/j.gca.2022.04.029.
[141] E. Salerno, F. Bühler, P. Bochsler, H. Busemann, M.L. Bassi, G.N. Zastenker, Y. N. Agafonov, N.A. Eismont, Measurement of $^3He/^4He$ in the local interstellar medium: The collisa experiment on Mir, Astrophys. J. 585 (2) (2003) 840, https://doi.org/10.1086/346203.
[142] B.H. Lodhia, L. Peeters, E. Frery, A review of the migration of hydrogen from the planetary to basin scale, J. Geophys. Res. Solid Earth 129 (6) (2024) e2024JB028715, https://doi.org/10.1029/2024JB028715.
[143] G. Etiope, Natural hydrogen extracted from ophiolitic rocks: a first dataset, Int. J. Hydrogen Energy 78 (2024) 368–372, https://doi.org/10.1016/j.ijhydene.2024.06.292.
[144] L. Truche, F.V. Donzé, E. Goskolli, B. Muceku, C. Loisy, C. Monnin, H. Dutoit, A. Cerepi, A deep reservoir for hydrogen drives intense degassing in the bulqizë ophiolite, Science 383 (6683) (2024) 618–621, https://doi.org/10.1126/science.adk9099.